1

Fundamentals of Orbital Angular Momentum Beams

Concepts, Antenna Analogies, and Applications

Anastasios Papathanasopoulos and Yahya Rahmat-Samii

Department of Electrical and Computer Engineering, University of California, Los Angeles, CA, USA

1.1 Electromagnetic Fields Carry Orbital Angular Momentum

Angular momentum is the rotational equivalent of linear momentum. An object moving in a straight line carries linear momentum. Along with its linear motion, an object can also rotate in two distinct ways. A spinning object carries spin angular momentum (SAM) and an orbiting object carries orbital angular momentum (OAM), with Earth being an interesting example for consideration. The analogy between the angular momentum of a moving object and the electromagnetic wave's angular momentum is shown in Figure 1.1. Earth's spinning is associated with SAM; Earth's orbital motion around the sun is linked to OAM. Electromagnetic beams may also carry these two types of momenta. If the electric field vector rotates along the beam axis, the beam has SAM; if the electromagnetic field's wavefront is twisting, with the wave vector forming a helix, the beam has OAM.

The history of angular momentum dates back to the early twentieth century. The SAM of light was theoretically studied for the first time by Poynting in 1909 [1] and experimentally studied by Beth in 1936 [2]. SAM is intrinsic, since it does not depend on the choice of an axis, and it is only polarization dependent. If s is the SAM mode number, then $s = \pm 1$ corresponds to right- and left-hand polarized waves, and $s = 0$ corresponds to linearly polarized waves. Although the experimental demonstration of the exchange of angular momentum between circularly polarized beams and matter was performed more than 80 years ago, the work associated with light's angular momentum has been almost exclusively concerned with SAM.

It was not until 1992 that Allen et al. [3] showed that helically phased beams with a phase term $e^{jl\phi}$ (where $j = \sqrt{-1}$ is the imaginary unit, l is the OAM mode number, and ϕ is the azimuthal angle) carry OAM. The wavefront of an OAM beam is a spiral; the phase twists around the beam axis and changes $2\pi l$ after a full turn. Unlike SAM, OAM is linked to spatial distribution rather than polarization. OAM is extrinsic, since it depends on the choice of the calculation axis. The angular momentum is the composition of SAM and OAM, such that the angular momentum mode number is $j = s + l$.

Electromagnetic Vortices: Wave Phenomena and Engineering Applications, First Edition.
Edited by Zhi Hao Jiang and Douglas H. Werner.

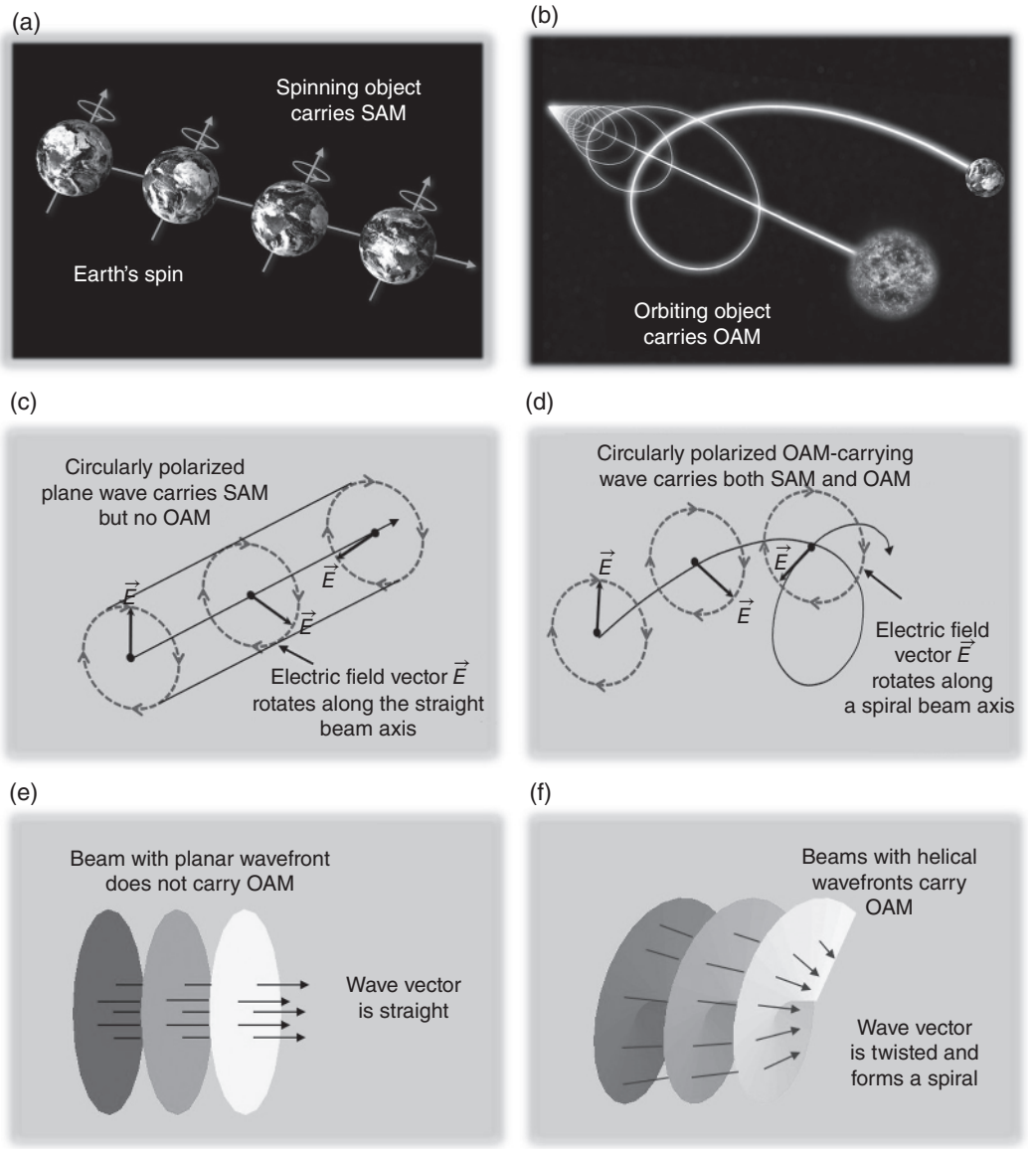

Figure 1.1 Analogy between moving object's and electromagnetic wave's angular momentum: (a) Earth spins and carries SAM; (b) Earth orbits around the sun and carries OAM; (c) a circularly polarized wave carries SAM; the electric field vector rotates along a straight beam axis; (d) a circularly polarized OAM-carrying wave carries both SAM and OAM; the electric field vector rotates along a spiral beam axis; (e) beam with planar wavefront; the wavevector is straight; (f) OAM-carrying beams with spiral wavefront; the wavevector is twisted.

1.2 OAM Beams; Properties and Analogies with Conventional Beams

Helically phased beams exhibit two unique properties: (i) the *orthogonality* of different OAM modes and (ii) the OAM beam *divergence*. As we will discuss in Section 1.3, the infinite number of orthogonal OAM modes provides an additional set of data carriers, thus OAM has the potential to increase

the capacity and spectral efficiency of wireless communication links [4]. The beam divergence can be advantageous for applications that require cone-shaped patterns, such as satellite-based navigation and guidance systems that serve moving vehicles [5] but may also pose a challenge for long-distance communication links [6]. In the subsequent paragraphs, these two peculiar features are explicated, and a comparative study between conventional and OAM beams is performed to underline their differences.

The first characteristic property of OAM beams is the *orthogonality* of distinct OAM modes. In general, the electric field of an OAM beam can be written as:

$$E(\rho, \phi, z) = A(\rho, z)e^{jl\phi}, \tag{1.1}$$

where ρ is the radial distance, ϕ is the azimuthal angle, and z is the propagation distance in the cylindrical coordinate system. There exist various subsets of OAM-carrying beams, for example Laguerre–Gaussian [3], Bessel–Gaussian [7], hypergeometric–Gaussian [8], vector vortex [9], and other beams [10]. The radial distribution $A(\rho, z)$ in Eq. (1.1) defines the special subset among all OAM-carrying beams. All the previous beams carry the $e^{jl\phi}$ term, which gives rise to an OAM mode of l-order. If we consider the electric fields $E_1(\rho, \phi, z)$, $E_2(\rho, \phi, z)$ of two OAM beams with modes l_1, l_2, and radial distributions $A_1(\rho, z)$, $A_2(\rho, z)$, the following orthogonality relation is satisfied [11]:

$$\int_0^{2\pi} E_1(\rho, \phi, z)E_2^*(\rho, \phi, z)d\phi = \begin{cases} 0 & \text{if } l_1 \neq l_2 \\ A_1(\rho, z)A_2^*(\rho, z) & \text{if } l_1 = l_2 \end{cases}, \tag{1.2}$$

where the asterisk (*) denotes the complex conjugate. It follows that: (i) there is an infinite number of OAM modes, with each mode identified by the mode number l, and (ii) the infinite set of OAM states forms an orthogonal basis.

The second special feature of OAM beams is the beam *divergence*. The far-field signature of the helical wavefront is an amplitude null at the phase vortex center. Accordingly, the null size can be described in terms of a divergence angle, which represents the angle from the null to the maximum gain [12]. As the OAM beam travels through space, the radius of the 'dark zone' around the amplitude null in the center of the beam increases.

1.2.1 Laguerre–Gaussian Modes

In general, an OAM-carrying beam could refer to any beam that carries the $e^{jl\phi}$ term, regardless of the radial distribution $A(\rho, z)$ in Eq. (1.1). The Laguerre–Gaussian modes are a special subset among all OAM-carrying beams that are cylindrically symmetric solutions to the paraxial wave equation in the cylindrical coordinate system [3]. The Laguerre–Gaussian modes are chosen to be presented because they are one of the most popular examples of OAM-carrying beams (see, for example [13–18]), and a general OAM-carrying beam can be expanded in a complete basis of Laguerre–Gaussian modes [11, 19, 20]. The electric field of a linearly polarized Laguerre-Gaussian beam at $z = 0$ can be written as [3, 5]:

$$\vec{E}^{LG}(\rho, \phi, z = 0) = \sqrt{\frac{2p!}{\pi(p + |l|)!}} \frac{E_0^{LG}}{w_g} \left(\frac{\rho\sqrt{2}}{w_g}\right)^{|l|} e^{-\rho^2/w_g^2} L_p^{|l|}\left(\frac{2\rho^2}{w_g^2}\right) e^{-jl\phi}\hat{x}, \tag{1.3}$$

where ρ and ϕ are the radial and azimuthal coordinates in the cylindrical coordinate system; E_0^{LG} is a complex amplitude coefficient, l and p are integers known as azimuthal and radial mode numbers, w_g is the equivalent beam waist that can be related to the antenna aperture diameter D (refer to [5]

and Appendix 1.A for more details) and is equal to the half-width of the normalized aperture field amplitude at $1/e$ controlling the transverse extent of the beam, $L_p^l(\cdot)$ is the associated Laguerre polynomial [21]:

$$L_p^l(x) = \frac{1}{p!} e^x x^{-l} \frac{d^p}{dx^p}\left(e^{-x} x^{p+l}\right) = \sum_{m=0}^{p} (-1)^m \binom{p+l}{p-m} \frac{x^m}{m!}, \tag{1.4}$$

where the binomial coefficient is [21]:

$$\binom{n}{k} = \frac{n!}{k!(n-k)!} \tag{1.5}$$

when $k \le n$ and is zero when $k > n$. For $l = 0$, the Laguerre–Gaussian beam carries no OAM since the phase term $e^{-jl\phi}$ vanishes. For any other l, the field carries the phase term $e^{-jl\phi}$, which gives rise to an OAM state of $-l$-order. The normalized electric field intensity distributions of Laguerre–Gaussian beams with different azimuthal and radial modes l and p are shown in Figures 1.2 and 1.3. It can be observed that the number of side lobe intensity rings is equal to the integer p. For the same p, the null size (i.e. the divergence angle) increases as the azimuthal mode number l increases.

The far-field features of Laguerre–Gaussian beams were studied in [5]. The far-field expression can be found from Eq. (1.3) using the aperture field method [5] (see Appendix 1.A for the proof):

$$\begin{aligned} \vec{E}_{ff}^{LG}(r,\theta,\phi) = {} & \frac{jk_0 E_0^{LG} e^{-jk_0 r}}{4\pi r}\left(\hat{\theta}\cos\phi - \hat{\phi}\cos\theta\sin\phi\right) w_g (-1)^p (-j)^l \\ & \times \sqrt{\frac{2\pi p!}{(p+|l|)!}} \left(\operatorname{sgn}(l)\frac{\Psi}{\sqrt{2}}\right)^{|l|} e^{-\Psi^2/4} L_p^{|l|}\left(\frac{\Psi^2}{2}\right) e^{-jl\phi} \end{aligned} \tag{1.6}$$

and $\Psi = k_0 w_g \sin\theta$ ($k_0 = 2\pi/\lambda$ is the free-space wavenumber). Equation (1.6) is a cone-shaped pattern with azimuthal symmetry. Note that the electric field maintains the phase term $e^{-jl\phi}$ in the far-field. This is a general characteristic of OAM fields (for example, the same feature is observed for the case of Bessel–Gaussian beams [5]) and a proof can be found in Appendix 1.A. The far-field expression for the Laguerre–Gaussian mode with $p = 0$ can be simplified as:

$$\vec{E}_{ff}^{LG}(r,\theta,\phi) = \frac{jk_0 E_0^{LG} e^{-jk_0 r}}{4\pi r}\left(\hat{\theta}\cos\phi - \hat{\phi}\cos\theta\sin\phi\right) w_g (-j)^l \sqrt{\frac{2\pi}{|l|!}} \left(\frac{\operatorname{sgn}(l)\Psi}{\sqrt{2}}\right)^{|l|} e^{-\Psi^2/4} e^{-jl\phi}.$$

For the dominant radial mode $p = 0$, the far-field expression Eq. (1.7) peaks at the elevation angle of:

$$\theta_c^{LG} = \frac{1}{\sin}\left(\frac{\sqrt{2|l|}}{k_0 w_g}\right). \tag{1.7}$$

Equation (1.7) shows that the cone angle depends both on the azimuthal mode number l and the beam waist (i.e. aperture diameter, as was shown in [5]). For constant l, the cone angle decreases as we increase the beam waist w_g, i.e. the aperture diameter. For constant w_g, the cone angle increases as we increase the mode number l.

In what follows, a comparison between two classes of beams is carried out. The first is the conventional Airy disk, and the second is the OAM-carrying Laguerre–Gaussian beam. The Airy disk pattern is produced by a circular aperture with uniform amplitude and phase-field distributions and it is a common and useful model in the design of conventional aperture-type antennas, such as

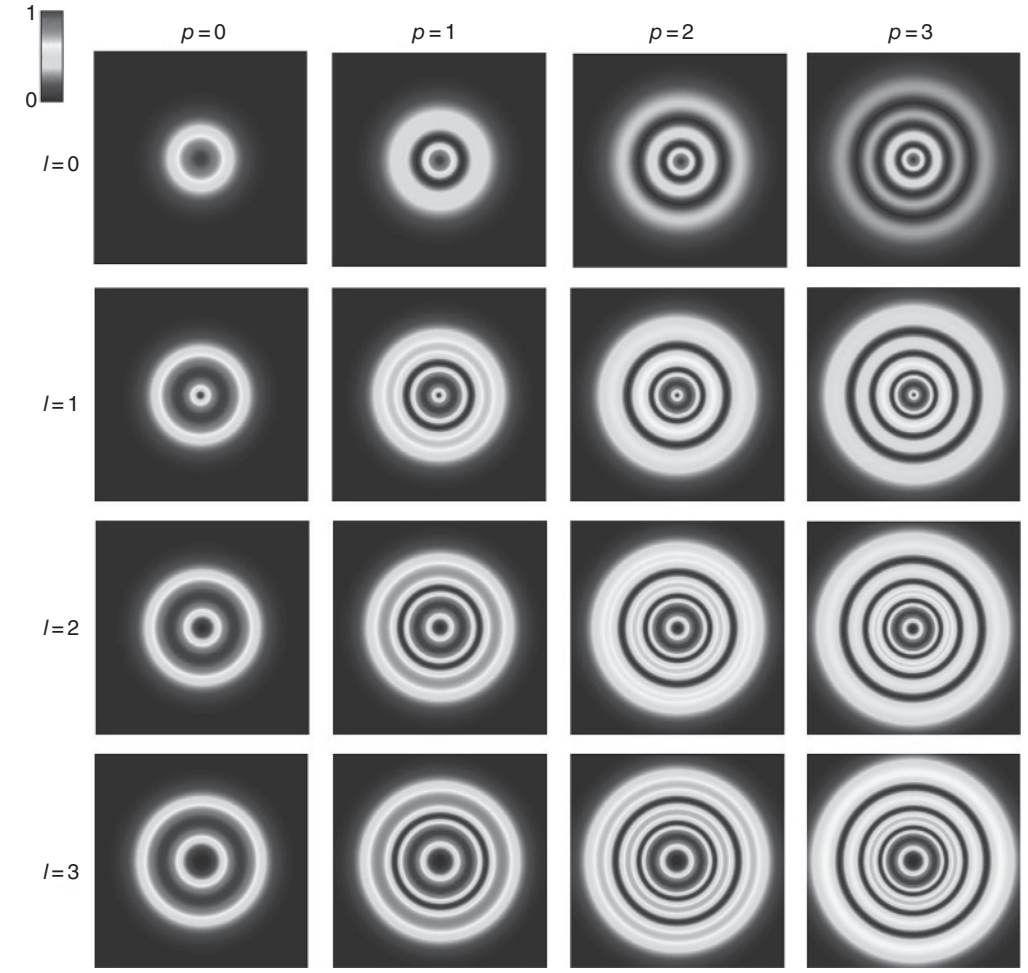

Figure 1.2 Normalized aperture field intensity distributions versus ρ/w_g of Laguerre–Gaussian beams with different azimuthal and radial modes l and p. The number of side lobe intensity rings is equal to the integer p. For the same p, the null size (i.e. the divergence angle) increases as the azimuthal mode number l increases.

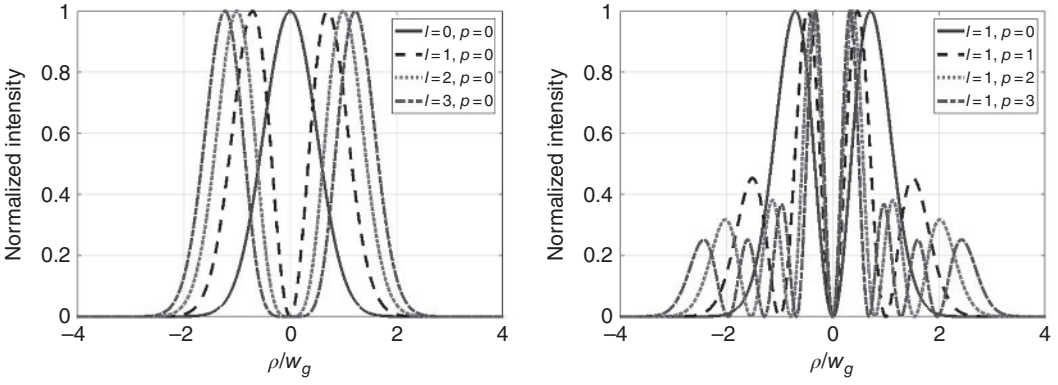

Figure 1.3 Normalized aperture field intensity line cuts of Laguerre–Gaussian beams with different azimuthal and radial modes l and p.

reflectors. The far-field electric field of the Airy disk pattern can be written as (see Appendix 1.A for the proof):

$$\vec{E}_{ff}^{AD}(r,\theta,\phi) = \frac{jk_0 E_0^{AD} a^2 e^{-jk_0 r}}{2r}\left(\hat{\theta}\cos\phi - \hat{\phi}\cos\theta\sin\phi\right)\frac{J_1(k_0 a\sin\theta)}{k_0 a\sin\theta}, \tag{1.8}$$

where E_0^{AD} is a constant; J_1 is the first-order Bessel function of the first kind; $k_0 = \frac{2\pi}{\lambda}$ is the free-space wavenumber; D is the aperture diameter, and $a = D/2$ is the radius of the aperture.

What are the fundamental differences between conventional and OAM beams? In the near-field region, the aperture phase of the Airy disk is uniform and the wavefront is planar. The Airy disk can be produced by a uniformly illuminated circular aperture antenna, such as a parabolic reflector antenna [22]. On the other hand, Laguerre–Gaussian modes can be produced by helicoidal reflector antennas [23]. The aperture phase of Laguerre–Gaussian modes twirls around the beam axis and changes $2\pi l$ after a full turn (l is the OAM mode number), resulting in a spiral wavefront. Figure 1.4 illustrates the analogies and antitheses between these two types of beams.

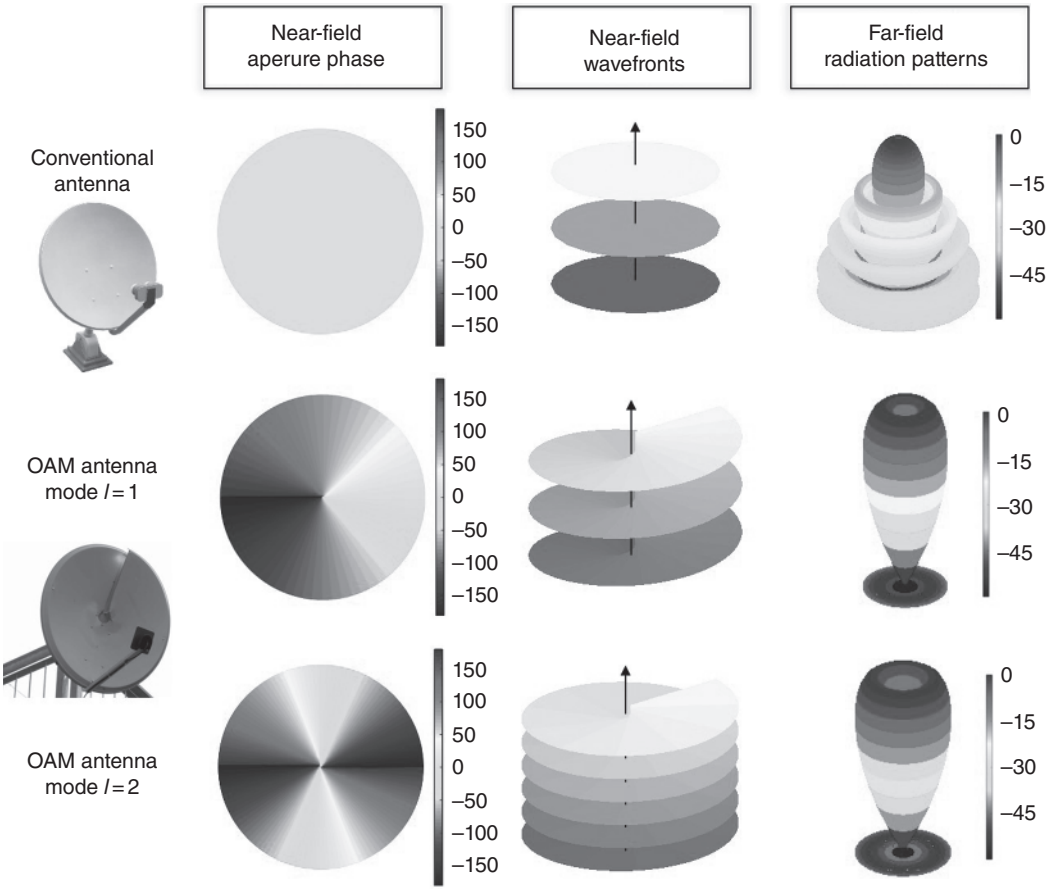

Figure 1.4 Comparison between conventional and OAM beams. A uniformly illuminated circular aperture produces a planar wavefront in the near-field and a highly directive far-field radiation pattern. An OAM-carrying Laguerre–Gaussian beam with mode number l produces a spiral wavefront in the near-field and a cone-shaped far-field pattern with an amplitude null at the phase vortex center. The OAM beam divergence increases for larger l.

The far-field characteristics of the Airy disk and the Laguerre–Gaussian beam are remarkably different. For the Airy disk case, the manifestation of the uniform aperture phase and the planar wavefront is a highly directive far-field pattern with the maximum gain at the axis of symmetry of the antenna. The locus of the points with constant phase in the far-field, i.e. the far-field wavefront S of the Airy disk, can be found from Eq. (1.8):

$$S_{AD} = k_0 r, \tag{1.9}$$

which describes a spherical wavefront. The gradient of the wavefront gives the direction of the wavevector (i.e. the geometrical optics ray direction):

$$\nabla S_{AD} = k_0 \hat{r} \tag{1.10}$$

For the Laguerre–Gaussian beam, the far-field signature of the vortex phase is a cone-shaped pattern with an amplitude null at the center. The locus of the points with constant phase in the far-field can be found from Eq. (1.6) and is described by the following equation:

$$S_{LG} = k_0 r + l\phi, \tag{1.11}$$

which describes a twisted wavefront, as shown in Figure 1.5. Note that the first term is frequency dependent similar to Eq. (1.10). The gradient of the wavefront (i.e. the wavevector direction) is:

$$\nabla S_{LG} = k_0 \hat{r} + \hat{\phi} \frac{l}{r \sin\theta} = k_0 \left[\hat{r} + \hat{\phi} \frac{l}{k_0 r \sin\theta} \right]. \tag{1.12}$$

Unlike the wavevector of the Airy disk, the wavevector of a Laguerre–Gaussian beam has a radial and azimuthal component. Note that for very large distances compared to the wavelength ($k_0 r \to \infty$),

$$\nabla S_{LG} \approx k_0 \hat{r}, \quad \text{for} \quad k_0 r \to \infty . \tag{1.13}$$

In other words, the wavefront of a Laguerre–Gaussian modes at very large distances compared to the wavelength, i.e. in the very far-field, resembles a spherical wavefront, as shown in Figure 1.5.

An immediately remarkable trait of the cone-shaped far-field pattern is the reduced directivity compared to the conventional beam counterpart. The Airy disk pattern is a highly directive far-field pattern with 100% aperture efficiency. A Laguerre–Gaussian mode with $l = 1$, aperture diameter D, and beam waist $w_g = 0.415D$ has an aperture efficiency of 50%. As a result, an antenna with an aperture that is twice as large compared to the conventional counterpart is required to maintain the same directivity level. Figure 1.6 shows the directivity of the Airy disk pattern and the first-order

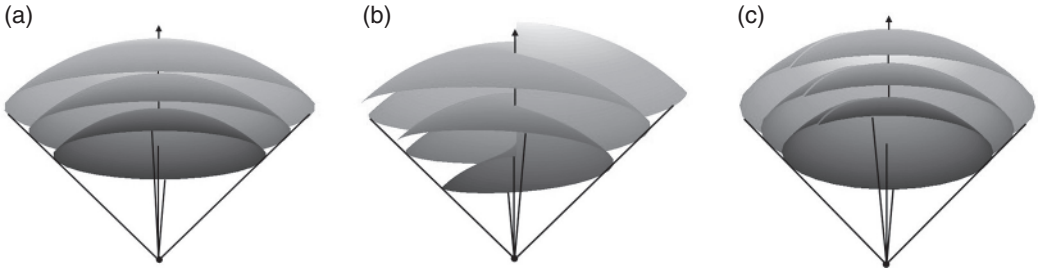

Figure 1.5 Far-field wavefront of (a) Airy disk and (b, c) Laguerre–Gaussian modes. The wavefront of the Airy disk is spherical and the wavefront of Laguerre–Gaussian modes is twisted; (c) at very large distances compared to the wavelength ($k_0 r \to \infty$), the wavefront of Laguerre–Gaussian approaches a spherical wavefront.

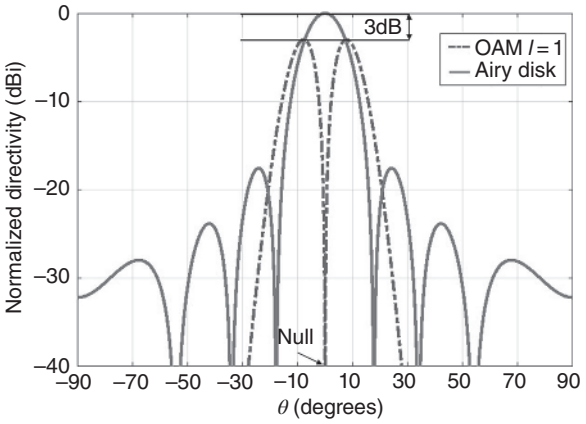

Figure 1.6 Normalized directivities of the Airy disk pattern with aperture diameter $D = 4\lambda$ and the Laguerre–Gaussian mode with mode number $l = 1$, same aperture diameter D, and beam waist $w_g = 0.415D$. The directivity of the Laguerre–Gaussian beam is 3 dB less than the Airy disk pattern for this choice of D and w_g. The curves are normalized to the maximum directivity of the Airy disk pattern.

Laguerre–Gaussian beam for $D = 4\lambda$ and $w_g = 0.415D$, normalized to the maximum directivity of the Airy disk pattern. The directivity of the Laguerre–Gaussian beam is 3 dB less than the Airy disk pattern of the same aperture size. Another distinctive characteristic is the beam divergence; the larger the OAM mode number, the larger the cone angle of the beam. That is, higher-order OAM modes diverge more rapidly with propagating distance.

To provide further insight in the OAM field distribution at various distances far from the antenna, we studied the changes of amplitude pattern shape from the reactive near-field toward the far-field. The first case of study is a conventional reflector antenna with a uniform aperture phase and −10 dB edge taper. The aperture field distribution is modeled using the two-parameter (2P) model [22, eq. (16)] (for more details see Appendix 1.A), and the field at various distances is calculated using the Fresnel–Kirchhoff diffraction integral [24]. The second case of study is a helicoidal reflector [23]. The aperture field is modeled using the [22, eq. (16)] multiplied by the phase term $e^{-jl\phi}$, for $l = 1$. The aperture diameter for both cases is $D = 10\lambda$. The changes of amplitude pattern shape from the reactive near-field toward the far-field for the two cases is shown in Figure 1.7. The pattern is calculated at $r = 4.9\lambda, 24\lambda, 8000\lambda$ corresponding to the reactive near-field, radiating near-field and far-field regions [25]. It can be observed that the amplitude null at the vortex center is maintained at all distances.

1.3 Communicating Using OAM: Potentials and Challenges

The observation that OAM-carrying beams exhibit two unique properties compared to conventional beams, namely, the orthogonality and divergence, gives rise to the following question: Can OAM beams' unique characteristics potentially benefit communication links? We demonstrate that the answer is 'yes,' albeit there are still many challenges to overcome before OAM is employed in a practical application. Inspired by this question, we examine possible communication scenarios that involve OAM antennas, review potential applications of OAM beams in communication systems, and discuss technical challenges.

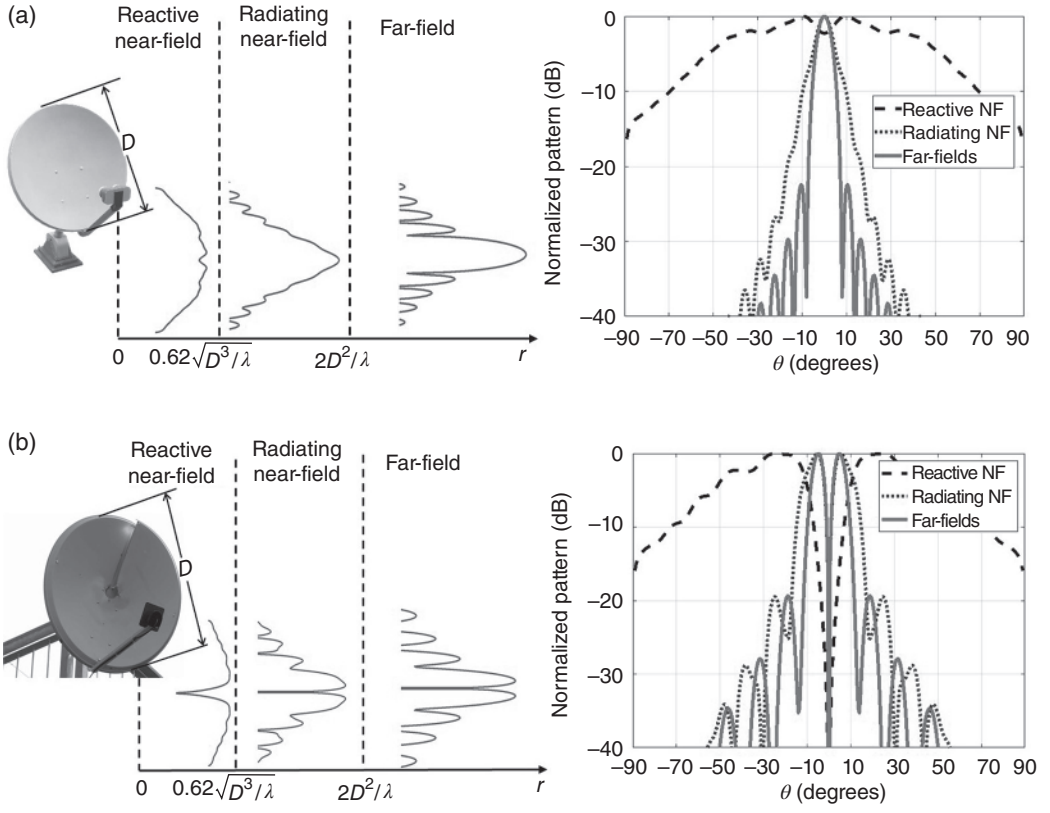

Figure 1.7 Changes of amplitude pattern shape from the reactive near-field toward the far-field for (a) a conventional antenna and (b) an OAM antenna. The dimensions are $D = 10\lambda$ and the pattern is calculated at $r = 4.9\lambda, 24\lambda, 8000\lambda$ corresponding to the reactive near-field, radiating near-field and far-field regions.

1.3.1 OAM Communication Link Scenarios and Technical Barriers

In general, there are two communication links that involve OAM antennas, as shown in Figure 1.8. In the first scenario, an OAM antenna establishes a communication channel with a conventional antenna (the OAM antenna can be transmitting or receiving signals). This case is no different than the classical counterpart, where two conventional antennas are utilized. The link budget is calculated using the classical Friis transmission formula based on the directional properties, distance in terms of wavelength, and orientation of the antennas [26]:

$$\frac{P_R}{P_T} = \left(\frac{\lambda}{4\pi d}\right)^2 G_T(\theta_t, \phi_t) G_R(\theta_r, \phi_r), \tag{1.14}$$

where P_R and P_T are the received and transmitted powers, respectively, λ is the operating wavelength, d represents the link distance, $G_T(\theta_t, \phi_t)$, $G_R(\theta_r, \phi_r)$ correspond to the gains along the transmitting T and receiving R antennas direction; antennas polarization mismatch is neglected for simplicity. The figure of merit of this communication link is the received power (i.e., signal-to-noise ratio) at the antenna terminals.

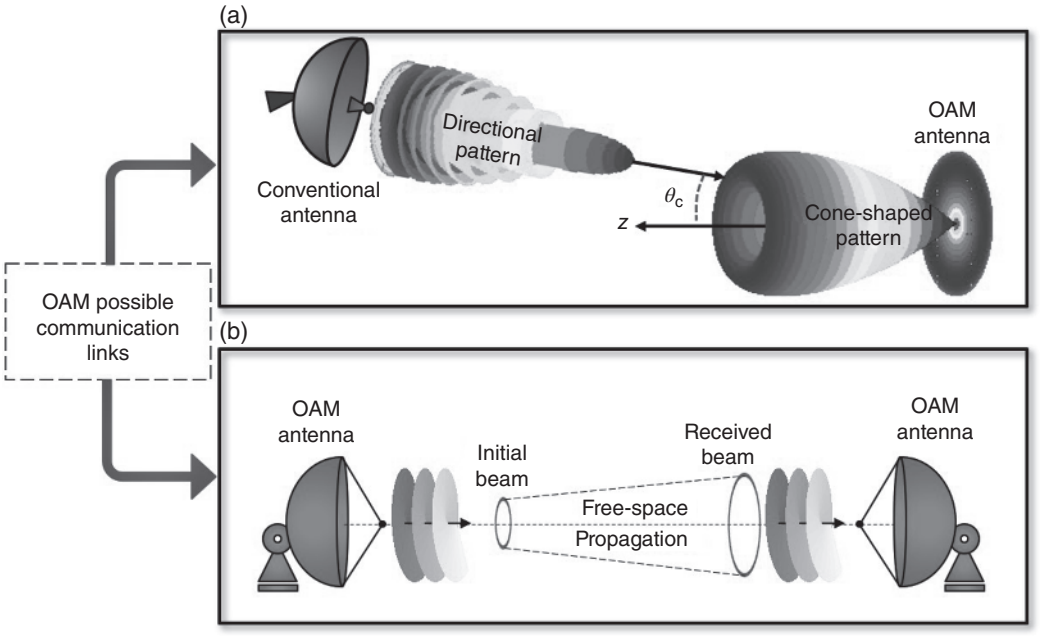

Figure 1.8 OAM possible communication links: (a) OAM to the conventional antenna. The figure of merit is the received power, which is calculated using the classical Friis transmission formula [26]. *Source:* Based on Friis [26]; (b) OAM to OAM antenna. The figures of merit are the received power and the detected OAM mode purity, which are calculated using the generalized Friis transmission equation [27]. The OAM beam divergence poses a challenge for far-field communication distances. A large receiving aperture is required. *Source:* Based on Cho and Byun [27].

In the second scenario, two OAM antennas that are facing each other constitute the communication link. The transmitting antenna generates an OAM beam of mode number l, which propagates in free space and is detected by another OAM antenna. The performance of this particular link is characterized by the received power (i.e., signal-to-noise ratio) as well as the detected OAM mode purity; a generalized Friis transmission equation that accounts for both the received power and the mode purity has been developed in [27]. A large receiving aperture is required for two reasons. First, a limited aperture would lead to power loss due to the central intensity drop of nonzero OAM modes. A series of recent studies has shown that the power loss penalty increases for larger OAM modes (larger OAM modes diverge more rapidly with propagating distance) [28–31]. Second, a substantial portion of the transmitted wavefront should be captured at the receiver endpoint to detect the OAM phase information and accurately estimate the mode number l.

An OAM-based communication link presents unique challenges that are related to the OAM beams' inherent characteristics, such as the beam divergence. Ideally, a large and perfectly aligned receiving aperture would capture the full OAM beam, as shown in Figure 1.9. The requirement to collect enough power of the divergent OAM beam with a very large aperture (compared to wavelength) significantly limits the achievable distance of OAM communication links [32], especially for the radio frequencies, where the wavelengths are longer compared to optical frequencies. In particular, Refs. [33–35] question the possibility of using OAM antennas in long-distance communication links. They highlight that to achieve a realistic signal-to-noise ratio at the receiver endpoint, the physical size of the receiving antenna becomes impractical. The impact of the finite receiving

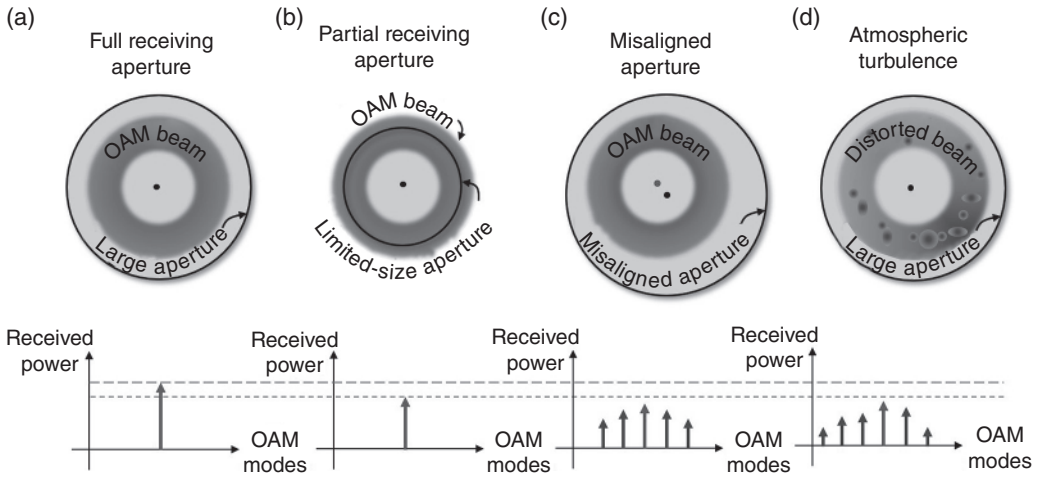

Figure 1.9 OAM communication challenges: (a) receiving with a perfectly aligned and full receiving aperture, (b) receiving with a limited-size aperture causes power loss of the detected mode, (c) receiving with a misaligned aperture, and (d) atmospheric turbulence causes power leakage in adjacent modes.

aperture size and the misalignment (lateral and angular) between the transmitter and the receiver on the performance of an optical OAM communication link was investigated in [36]. In principle, when a finite-size receiving aperture is used, power loss of the detected mode occurs (see Figure 1.9). Receiving an OAM beam with misalignment would cause power leakage in the neighboring modes and inter-mode crosstalk [37].

Another critical challenge for a practical OAM-communication link is the atmospheric turbulence. Temperature and pressure fluctuations in the atmosphere result in spatial changes in the refractive index. The propagation of optical OAM beams in the turbulent atmosphere has been numerically modeled in [38–40] and experimentally investigated in [41–45]. The main conclusion is that atmospheric turbulence leads to wavefront distortion and significant system performance degradation. Atmospheric turbulence impacts more OAM beams in optical frequencies than radio frequencies [32]. As the turbulence strength increases, the power of the transmitted OAM mode starts to leak to neighboring modes and tends to be equally distributed among modes for strong turbulence [46].

The multipath propagation phenomenon in wireless communication links using OAM is another factor that affects the system performance. The analysis, simulations, and measurements of multipath effects in a millimeter-wave communication link using OAM multiplexing at 28 GHz were presented in [47]. A schematic of multipath effects of an OAM channel caused by specular reflection from a parallel ideal reflector (ground plane) that is placed at distance h below the transmitting antenna is shown in Figure 1.10. From image theory, the reflected beam can be seen as an OAM beam of an opposite mode number (the reflection changes the sign of the OAM mode) that is placed at a distance h below the ground plane. As a result, the receiver antenna will not only receive an OAM beam with an OAM number of l from the original transmitter but also a reflected beam with an OAM number of $-l$ from an offset link. Ref. [47] showed that an OAM channel with a higher OAM number l tends to suffer more from both strong intra-channel crosstalk and strong inter-channel crosstalk with other OAM channels.

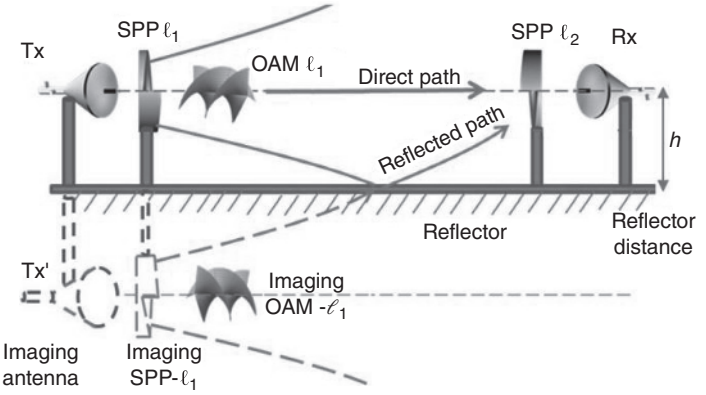

Figure 1.10 A schematic of multipath effects of an OAM channel caused by specular reflection from a parallel ideal reflector (ground plane) that is placed at distance *h* below the transmitting antenna. The receiver antenna will not only receive an OAM beam with an OAM number of *l* from the original transmitting antenna but also a reflected beam with an OAM number of −*l* from an offset link. *Source:* Yan et al. [47]; © 2016 Springer Nature. Licensed under CC BY-4.0.

1.3.2 OAM Emerging Applications and Perspectives

1.3.2.1 Free-space Communications

One application that may take advantage of the OAM cone-shaped pattern is the local satellite-based navigation and guidance system that serves moving vehicles. For such an application, the satellite is usually placed in a geostationary orbit and employs a contour beam that covers a certain geographical area [5], as shown in Figure 1.11. An antenna is mounted on the moving vehicle and is circularly polarized to alleviate multipath propagation problems caused by reflections from building walls and the ground surface. For the vehicle to continuously communicate with the satellite, a directivity of at least 3 dB in the direction of the satellite should be maintained regardless of the orientation of the vehicle [48].

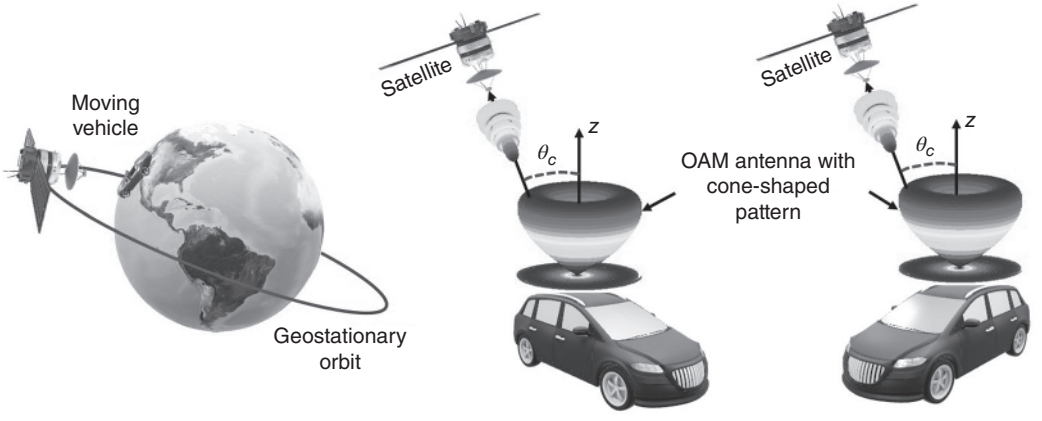

Figure 1.11 A satellite-based, geostationary navigation and guidance system that serves moving vehicles. OAM antennas with cone-shaped patterns are proposed to be mounted on the vehicle [5]. The same signal-to-noise ratio is achieved regardless of the orientation of the vehicle because of the horizontally omnidirectional radiation pattern. *Source:* Modified from Veysi et al. [5].

Several antenna designs have been suggested for communications between moving vehicles on the earth and geostationary satellites. One possible solution is an antenna with a pencil-beam pattern that sweeps out a cone in space. The beam pattern scans to continuously point toward the satellite so that uninterrupted vehicle-to-satellite communication is achieved. This solution increases the cost of the antenna system since the tracking of the satellite is needed. An alternative approach is an antenna with a fixed cone-shaped pattern, with the peak of the cone (denoted by the cone angle θ_c in Figure 1.11) pointing toward the satellite. The same signal-to-noise ratio is achieved regardless of the orientation of the vehicle because of the horizontally omnidirectional radiation pattern. The latter approach does not require the tracking of the satellite, thus the antenna cost and complexity are reduced. Among various antennas with conical patterns that have been proposed for vehicle-to-satellite communications [48–51], an OAM antenna is a powerful apparatus that systematically generates a cone-shaped pattern with high-azimuthal symmetry [5].

Besides the OAM beam divergence and the cone-shaped pattern, the second fundamental property of OAM beams, namely, the orthogonality of different OAM modes, can be employed to transfer information. OAM shift keying (OAM-SK) is one communication technology that takes advantage of the distinction of the different orthogonal OAM modes [11, 32, 52, 53]. In this communication technology, the OAM modes are used as a communication alphabet, with N data symbols encoded in the OAM mode number l of N OAM states. Figure 1.12 shows an example where OAM modes $l = 0,\ 1,\ 2$ represent the data symbols 0, 1, 2. The sequence of the OAM states is sent by the transmitter. The data are decoded at the receiver by checking the received OAM mode number. OAM-SK is a direct modulation technology that enables transferring information by encoding information in the value l of the OAM mode number.

A series of proof-of-concept experiments has elevated the scientific interest in the potential of harnessing OAM-SK for free-space information transfer. The first experiment to use OAM-SK for free-space information transfer was carried out by Gibson in 2004 [17]. In Gibson's seminal work, eight different OAM modes in the set $\ell = \{-16,\ -12,\ -8,\ -4,\ +4,\ +8,\ +12,\ +16\}$, each representing a data symbol, were used as communication alphabets. The transmitted OAM states and data symbols were accurately measured up to a transmission range of 15 m using a HeNe laser transmitter at a wavelength of 632.8 nm. Since the pioneering work of Gibson, several OAM-SK experiments have been carried out. In [54], 16 superimposed OAM modes were used to transfer information over a 3 km link of strong turbulence over the city of Vienna. The transmitter was a laser with a spatial light modulator at a wavelength of 532 nm. An incoherent detection scheme aided by an artificial neural network was employed to identify the characteristic mode patterns and distinguish among the 16 OAM modes. The latter experimental scheme has been extended to a distance of 143 km between two Canary Islands [55]. To the authors' best knowledge, this is the longest distance that an OAM-SK experiment has been reported. Therein, the OAM mode

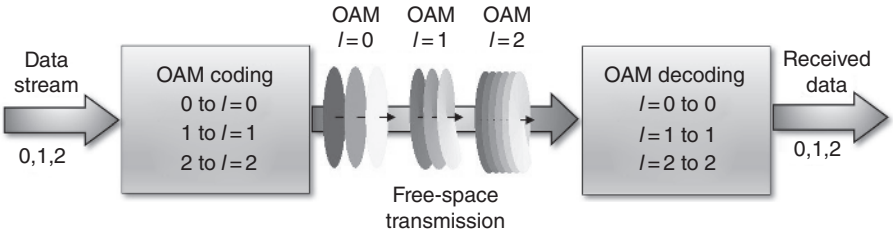

Figure 1.12 OAM shift keying (OAM-SK) modulation. OAM-SK takes advantage of the distinction of the different orthogonal OAM modes. The data symbols 0, 1, 2 are encoded in the OAM mode number l = 0, 1, 2.

patterns were observed on a receiving aperture with a diameter of roughly $D = 11$ m, and a green laser with a wavelength of 532 nm was used, corresponding to a far-field distance of $2D^2/\lambda = 4.55 \times 10^5$ km. Note that the 143 km link distance is large in absolute terms, but it cannot be considered a far-field distance. As discussed in Section 1.3.1, objections regarding the possibility of using OAM in far-field communication links have surfaced in [33–35], and the adoption of OAM in far-field wireless communications is still an open problem.

As the available wireless spectrum becomes more and more crowded under the incessant strive for high data-transfer capacities, several methods have been developed to increase the spectral efficiency. Various properties of the electromagnetic wave, such as time, polarization, and wavelength, have been employed to develop multiplexing schemes [56, 57]. Using the spatial property of electromagnetic waves as a new dimension (i.e. space division multiplexing (SDM)) has recently aroused interest as a potential method to enhance wireless communications. A special case of SDM is the mode division multiplexing (MDM), where spatially orthogonal modes act as independent data channels that can be efficiently multiplexed and de-multiplexed. Thereby, the spectral efficiency is increased by a factor equal to the number of the independent spatial modes.

One particular subset of SDM is the OAM division multiplexing (OAM-DM) [32]. In an attempt to further increase the spectral efficiency of wireless communications, OAM-DM technique exploits the orthogonality of OAM modes [58, 59]. An independent data stream (i.e. data 1, 2, ..., N in Figure 1.13) is encoded on the value l of N carrier OAM modes. The different OAM beams are multiplexed at the transmitter along with other modes, propagate through a common medium, and are de-multiplexed at the receiver. The obtained field at the receiver can be written as [32]:

$$U_{\mathrm{MUX}}(\rho, \phi) = \sum_{p=1}^{N} S_p A_p(\rho) e^{jl_p\phi}, \tag{1.15}$$

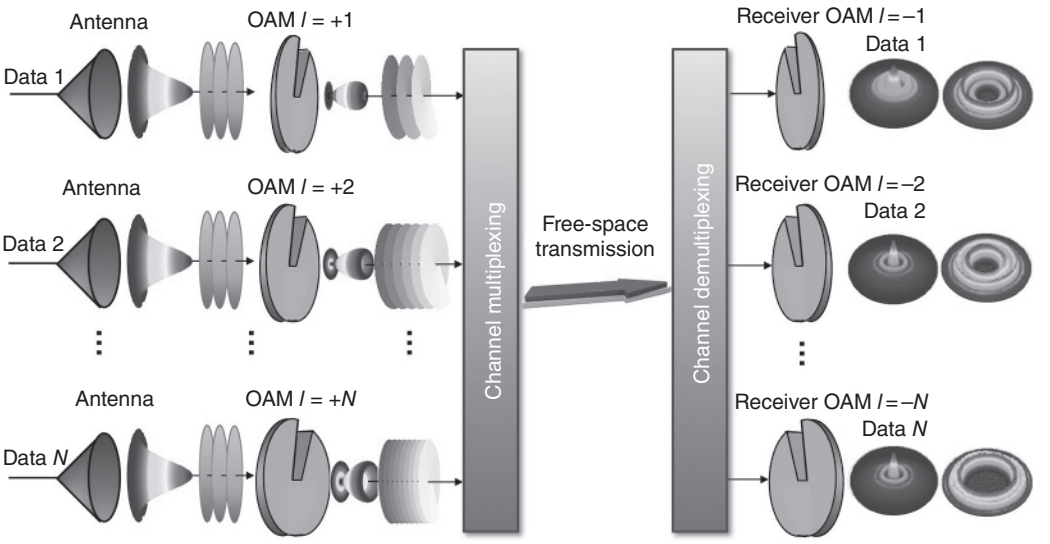

Figure 1.13 OAM division multiplexing (OAM-DM) modulation. An independent data stream (i.e. data 1, 2, ..., N) is encoded on the value l of N carrier OAM modes. The different OAM beams are multiplexed at the transmitter, propagate through a common medium, and are de-multiplexed at the receiver. Thereby, the spectral efficiency is increased by a factor N equal to the number of the carrier OAM modes.

where N is the number of OAM modes, S_p is the modulated data signal on the pth OAM mode, $A_p(\rho)$ is the complex electric field amplitude of the pth OAM mode, ρ is the radial distance, and ϕ is the azimuthal angle in the cylindrical coordinate system. At the receiver end, the multiplexed signal is multiplied by a phase factor $e^{-jl_q\phi}$, where $l_q = 1,\ 2,\ ...,\ N$. The OAM beam with $l = l_q$ has a central intensity peak and can be easily distinguished from other modes by means of their different spatial signatures. Finally, the data information carried by the OAM mode $l = l_p$ can be retrieved. Consequently, the spectral efficiency is increased by a factor N equal to the number of the carrier OAM modes. A schematic diagram illustrating the principles of OAM-DM is shown in Figure 1.13.

Several recent experiments have demonstrated the potential of optical OAM multiplexing to increase the spectral efficiency of wireless communication systems. In [61], a transmission capacity of 2.56 Tbit s^{-1} and a spectral efficiency of 95.7 bit s^{-1} Hz^{-1} were achieved using OAM-DM and polarization multiplexing (8 OAM modes and 2 orthogonal polarization states at a wavelength of 1550.12 nm). In [60], an aggregate capacity of 100.8 Tbit s^{-1} was achieved using 1008 data channels. Each data channel was carried on 12 OAM beams, 2 polarizations, and 42 wavelengths (1536.34–1568.5 nm), and was encoded with 100 Gbit s^{-1} quadrature phase-shift keying data. A schematic illustrating the concept of three-dimensional multiplexing to increase the multiplexed data channels by combing OAM-DM, polarization-division multiplexing, and wavelength-division multiplexing is shown in Figure 1.14. OAM-DM can be combined with other multiplexing schemes, such as time, polarization, and wavelength multiplexing, to satisfy the ever-growing need for transmission capacity.

The possibility of using OAM-DM extends beyond optical frequencies. Thidé et al. [62] were the first to numerically show that antenna arrays can generate OAM beams in radio frequencies and highlight the potential of OAM communications in the lower frequencies. The first experimental test of encoding multiple channels on the same radio frequency using OAM was performed by Tamburini et al. [23]. Subsequently, several OAM-DM experiments have been performed in the radio frequency domain. In [63], an OAM-DM 10 m microwave link operated at 10 GHz with four OAM modes was experimentally demonstrated to quadruple the spectral efficiency while keeping a low-receiver computational complexity. The antenna aperture size was 0.6 m, which corresponds to a far-field distance of $2D^2/\lambda = 24$ m and the 10 m link cannot be considered a far-field link. In [64], a 32 Gbit s^{-1} mm-wave link was demonstrated over 2.5 m at a carrier frequency of 28 GHz with a spectral efficiency of 16 bit s^{-1} Hz^{-1} using four independent OAM beams on each of the two orthogonal polarizations. The receiving and transmitting antenna aperture had circular apertures with diameters of 30 cm, which correspond to a far-field distance of $2D^2/\lambda = 16.8$ m and the 2.5 m link cannot be considered a far-field link. As discussed in Section 1.3, the adoption of OAM in far-field wireless radio frequency (RF) communications is still an open problem.

1.3.2.2 Optical Fiber Communications

Optical fibers have been successfully integrated into communication systems, offering the advantages of large bandwidth, low loss and cost, and immunity to electromagnetic interference [65]. The conventional optical fiber is known as single-mode fiber (SMF) and includes a core surrounded by a transparent cladding material with a lower index of refraction; the attenuation is typically 0.2 dB/km at 1550 nm and the core radius does not exceed 10 μm [53]. Up to now, the increasing demand for high-speed data transfer in optical networks has been covered by the conventional SMF. The growing demand for network capacity is expected to continue in the future. According to Ref. [66], the annual global data center traffic will reach 20.6 Zettabytes (zB) – or 20.6×10^{21} bytes – (1.7 zB per month) by the end of 2021, up from 6.8 zB per year (568 exabytes per month) in 2016.

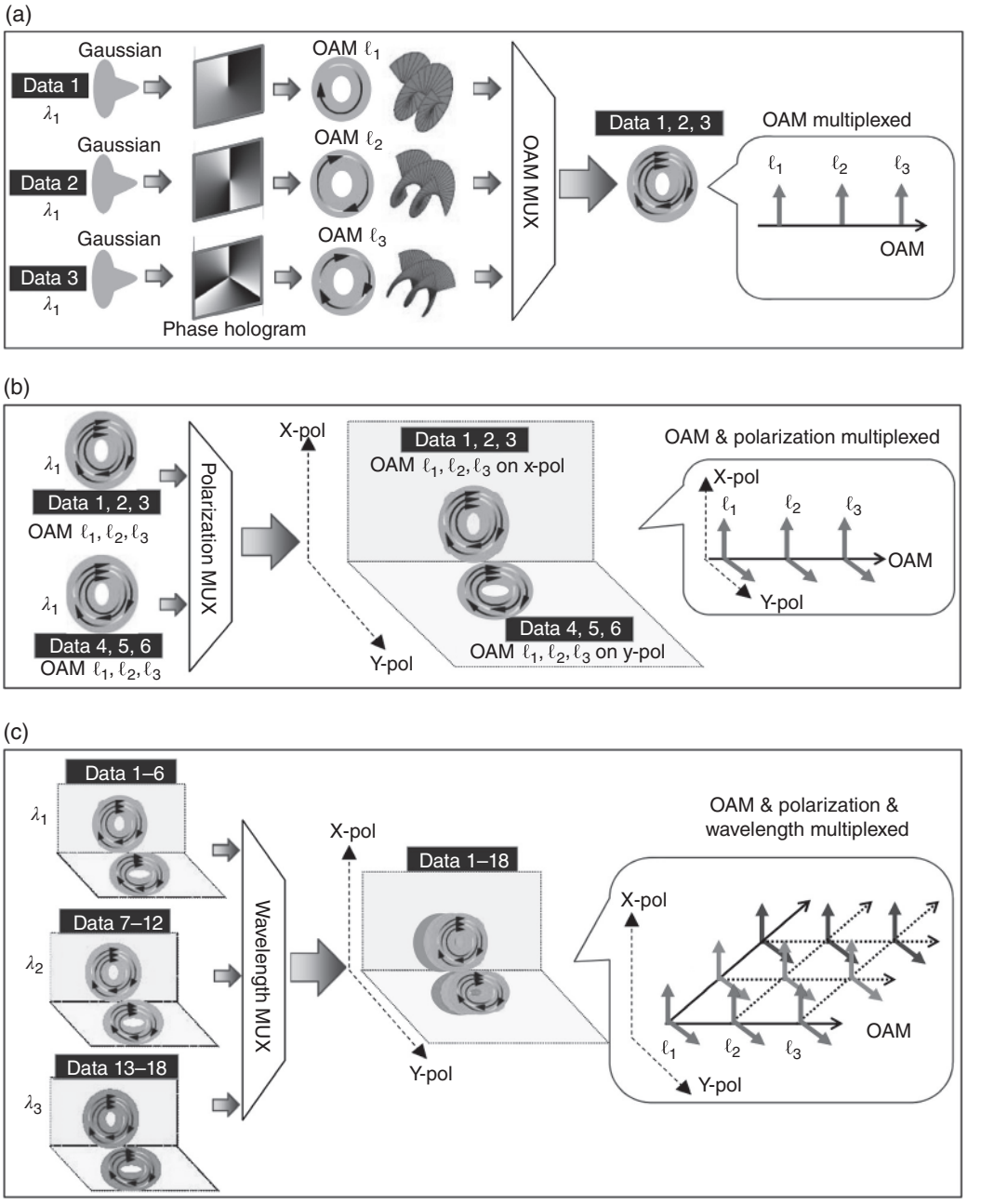

Figure 1.14 A schematic illustrating the concept of three-dimensional multiplexing to increase the multiplexed data channels by combing (a) OAM-DM, (b) polarization-division multiplexing, and (c) wavelength-division multiplexing. *Source:* Huang et al. [60] © 2014 Optical Society of America.

In an attempt to meet the everlasting demand for network capacity, alternative methods have been developed to increase the spectral efficiency of optical networks. The problem is that the conventional SMF has its inherent capacity limits; therefore, researchers have focused on innovative ways to increase the data-carrying capacity of a single optical fiber. SDM using multi-core fibers

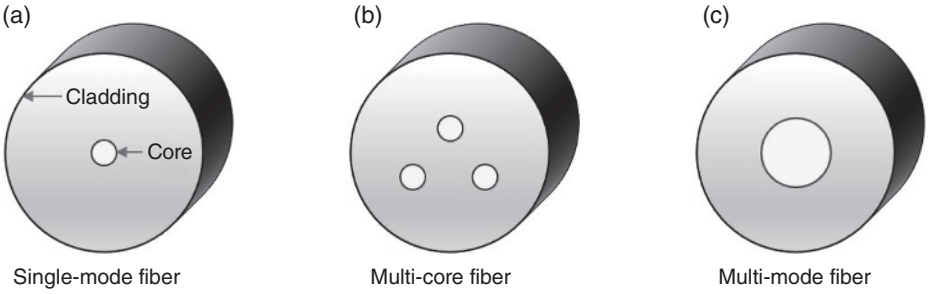

Figure 1.15 A schematic representation of different types of optical fibers.

(MCFs), multi-mode fibers (MMFs), and their combination has been considered to overcome the capacity crunch of conventional SMFs [67, 68]. A schematic of different types of optical fibers is shown in Figure 1.15 [65]. In an MCF, multiple cores share the same cladding and act as an independent data carriers; thereby, the spectral efficiency scales by the number of the cores. Unlike MCFs, MMFs have a single core that is larger than the conventional SMF, usually around 50 μm in radius. MMFs can support multiple spatial orthogonal modes each carrying distinct data and acting as a separate communication channel, thus increasing the spectral efficiency of optical fibers. The latter special case of SDM is known as MDM [67].

The most popular spatial modes for fiber MDM are the linearly polarized (LP) modes. LP modes are the superposition of the fiber eigenmodes transverse electric (TE), transverse magnetic (TM), and hybrid modes of HE and EH type [65]. LP modes are the solution of the scalar Maxwell's equations and propagate under the weakly guiding approximation, which is valid when the refractive indices of the core and the cladding are very close (within 1%) [69]. The intensity profiles of LP modes together with the constituent eigenmodes and the corresponding propagation constants β are shown in Figure 1.16a–d. The constituent eigenmodes of each LP mode have different propagation constants leading to walk-off and mode distortion. LP modes also share common eigenmodes and thus are inherently coupled during propagation leading to crosstalk. To overcome the problem of mode-coupling, MMFs rely on digital signal processing (DSP) algorithms based either on adaptive optics feedback or complex multiple-input multiple-output (MIMO) methodologies [32, 70].

To avoid inter-modal coupling and MIMO DSP complexity in MMFs, OAM modes have been proposed as an alternative modal basis set [69]. The electric field of OAM modes in fibers can be expressed in terms of HE and EH hybrid modes as [71, 72]:

$$\mathrm{OAM}_{\pm l,m} = \begin{cases} \mathrm{HE}^{\mathrm{even}}_{l+1,m} \pm j\mathrm{HE}^{\mathrm{odd}}_{l+1,m} \\ \mathrm{EH}^{\mathrm{even}}_{l-1,m} \pm j\mathrm{EH}^{\mathrm{odd}}_{l-1,m} \end{cases} \tag{1.16}$$

The intensity profiles of OAM modes, the constituent eigenmodes, and the corresponding propagation constants β are shown in Figure 1.16e–h. Unlike LP modes, OAM modes are formed by the superposition of a single eigenmode type with even and odd symmetry [73]. That is, OAM modes are inherently de-coupled resulting in low crosstalk, and the constituent eigenmodes with even and odd symmetry share the same propagation constant leading to a reduced walk-off effect compared to LP modes [74]. As a result, OAM has the potential to increase the spectral efficiency of optical fiber communications while obviating complex DSP algorithms.

OAM-based fiber communications is a new field of research with a short history. The first paper to report the generation of an OAM-carrying optical vortex in a fiber was published in 2006 [76].

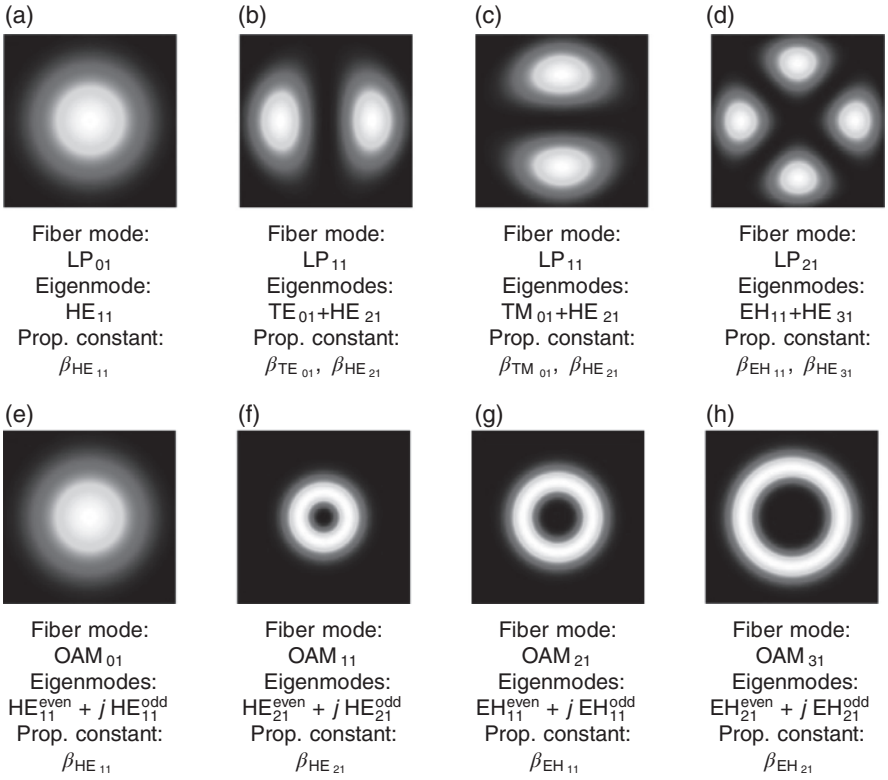

Figure 1.16 Intensity profiles of LP modes and OAM modes. The constituent eigenmodes and the propagation constants β of each mode are noted below each LP and OAM mode. Unlike OAM modes, LP modes (i) have distinct propagation constants leading to walk-off and (ii) share common eigenmodes and are inherently coupled resulting in crosstalk.

Bozinovic et al. reported the stable propagation of OAM modes in a new class of optical fibers, called *vortex fibers* [77, 78]. The vortex fiber of [78] maintained a mode purity of 97% after a propagating distance of 20 m at a wavelength of 1550 nm under bends and twists. The same group demonstrated the successful transmission of OAM states through a 0.9 km vortex fiber. In 2012, a 1.1 km long vortex fiber was presented [79]. A year later, the same 1.1 km vortex fiber was used to achieve 400 Gbit s^{-1} data transmission using four OAM modes at a single wavelength of 1550 nm, and 1.6 Tbit s^{-1} using two OAM modes over 10 wavelengths around 1550 nm with a low-complexity DSP coherent detection method [80]. The experiment of [80] suggested that OAM could provide an additional degree of freedom for data multiplexing in future fiber networks using OAM-MDM that does not require complex DSP [81]. At present, research efforts focus on the design of fibers that can support multiple OAM modes, both MMFs (see, for example Refs. [74, 82–85]) and MCFs (see Figure 1.17 and Refs. [75, 86, 87]).

1.4 OAM Generation Methods

The history of OAM dates back in 1992, when Allen et al. showed that helically phased beams with a phase term $e^{jl\phi}$ carry OAM [3]. Since then, research efforts have focused on the generation of OAM beams. Figure 1.18 shows the analogy between the generation principle of OAM and conventional

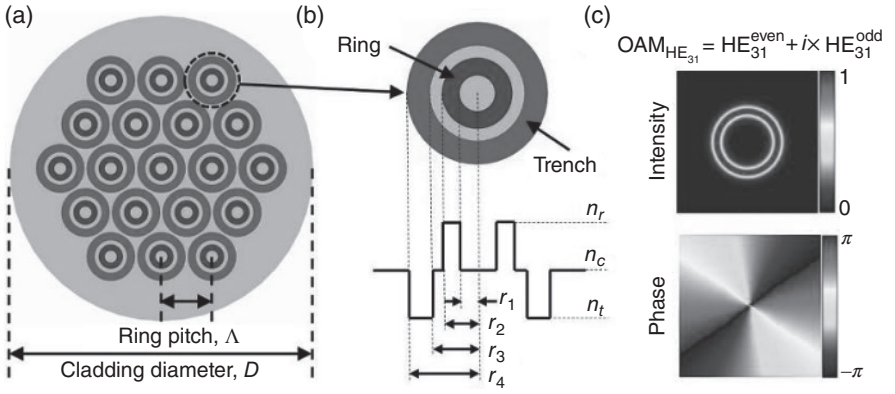

Figure 1.17 (a) Cross-section of a 19-ring multi-OAM multi-ring fiber. (b) Refractive index profile of a single ring. (c) Intensity and phase distributions of HE_{31} related OAM mode in a single ring. *Source:* Li and Wang [75] © 2014 Springer Nature.

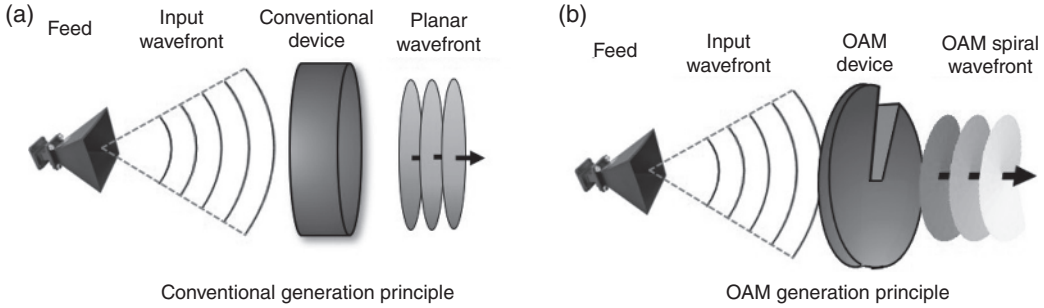

Figure 1.18 Analogy between conventional and OAM generation principle.

beams. In a conventional antenna system, a device (such as reflectors [22] and lenses [88]) is used to transform an input wavefront (for example, a spherical wavefront in Figure 1.18) into a planar wavefront, to achieve a highly directive beam in the far-field. In analogy with the conventional antenna system, an OAM system employs an OAM device to transform the input wavefront into a spiral wavefront. Figure 1.19 shows a representative example where the wavefront-transformation devices are a parabolic reflector [22] and a helicoidal reflector antenna [23], corresponding to the conventional and OAM cases, respectively. The conventional reflector antenna attempts to achieve a uniform phase in the exit aperture, whereas the helicoidal reflector aims to achieve the OAM vortex phase.

The generation of OAM-carrying beams necessitates the design of antennas that can generate the vortex aperture phase and spiral wavefront that are associated with OAM beams. Some representative designs that have been developed for this purpose are shown in Table 1.1. The spiral phase plate (SPP) has one planar and one spiral surface with a step discontinuity, and the thickness increases as the azimuth angle increases [13, 19, 89–91]. The original shape of the conventional parabolic reflector is modified to form a 'helicoidal reflector' [23] that converts the field generated by a feed into an OAM-carrying field [92–94]. A stepped spiral reflecting surface is a discrete approximation of the helicoidal reflector [101]. Planar SPPs, transmitarray [95–100], and reflectarray antennas [5, 114–117] employ elements that are distributed in planar surfaces; these elements

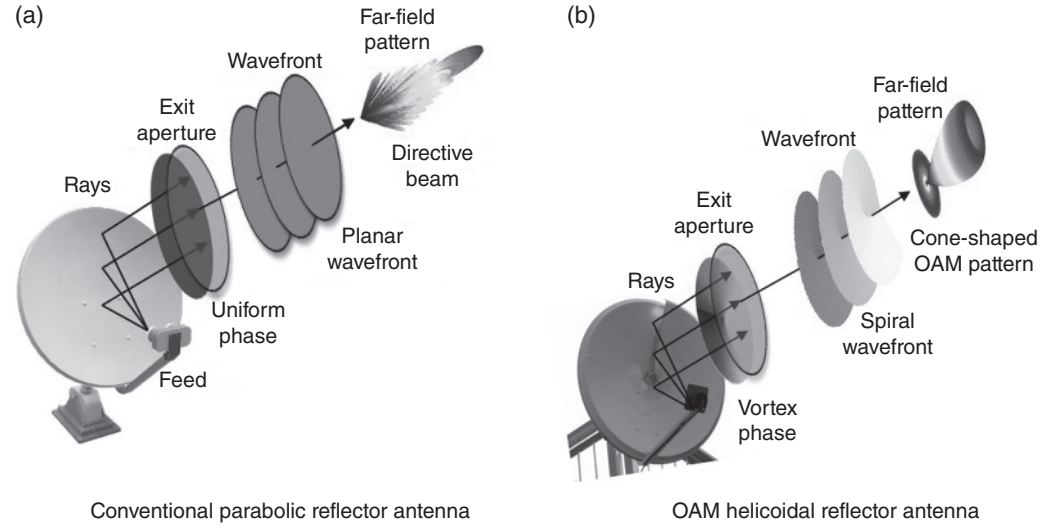

Figure 1.19 Comparison between the generation method of conventional antennas with directive far-field patterns and OAM antennas: the case of reflector antennas.

compensate the phase delay associated with incident waves from different paths emitted from the feed and generate the desired vortex phase distribution. The uniform circular array (UCA) consists of elements that are uniformly distributed on the circumference of a circle. The array elements are fed with an input signal with the same amplitude but with a successive phase delay from element to element such that after a full turn the phase has been incremented by $2\pi l$, where l is the OAM mode number [33, 62, 102–109]. The transmittance functions of holographic gratings can also be designed to generate OAM beams [110–113]. Other generation methods include cylindrical lenses [3], spatial light modulators [9], q plates [118], dielectric resonators [119], traveling-wave circular loops [120], and metasurfaces [121]. The previous designs can generate single-mode OAM beams, superposition of OAM modes, i.e., mixed-mode OAM beams [5, 95], and mode-reconfigurable OAM beams [102, 121].

1.5 Summary and Perspectives

This chapter has provided a comprehensive overview of OAM beams. We analyzed the fundamental properties of OAM beams and contrasted them with conventional beams. In addition, an appendix is provided to summarize the fundamental mathematical details when the OAM concept is used for potential antenna applications. We discussed emerging applications of OAM in free-space optical and RF communications as well as in fiber communications, highlighting potentials, and technical challenges. A comprehensive list of relevant references is included. We also summarized the generation methods of optical and RF OAM. Analogies regarding the fundamental properties, antenna communication links, and generation methods between OAM and conventional beams have been provided. More details on various aspects of OAM are discussed in various chapters of this book. We conclude by providing Table 1.2, which summarizes the theoretical and experimental milestones regarding OAM in chronological order. OAM is a field with short history of less than 30 years that has come a long way so far, and we are excited to see the future advancements of OAM.

Table 1.1 OAM generation methods and fabricated prototypes.

Generation method	Prototype photo	
Spiral phase plate (SPP) Refs.: [13, 19, 89–91] Optical and RF OAM	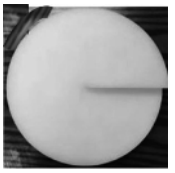	Photo credit: [90]
Helicoidal reflector antenna and reflector antenna systems Refs. [23, 92–94] RF OAM		Photo credit: [23]
Planar spiral phase plate and transmitarray antenna Refs. [95–100] RF OAM	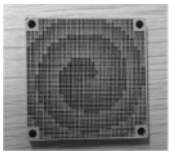	Photo credit: [95]
Stepped spiral reflecting surface Ref. [101] RF OAM	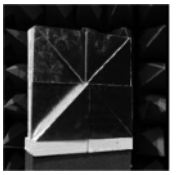	Photo credit: [101]
Uniform circular array (UCA) Refs. [33, 62, 102–109] RF OAM	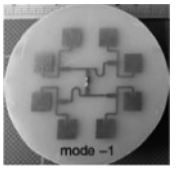	Photo credit: [102]
Holographic gratings Refs. [110–113] Optical and RF OAM	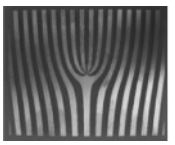	Photo credit: [110]
Reflectarray antennas Refs. [5, 114–117] RF OAM		Photo credit: [114]

Appendix 1.A OAM Far-field Calculation

The aperture field of an OAM-carrying linearly polarized field with a cylindrically symmetric distribution $E(\rho')$ can be written as:

$$\vec{E}(\rho', \phi') = E(\rho')e^{-jl\phi'}\hat{x}, \quad 0 < \rho' < a, \tag{1.A.1}$$

Table 1.2 Chronicle of milestones regarding OAM.

Reference	Year	Main contribution
[1]	1909	Theoretically studied angular momentum of circularly polarized waves
[2]	1936	Experimentally studied the SAM of light and demonstrated that SAM can cause the rotation of a mechanical system
[3]	1992	Recognized that light beams with an azimuthal phase dependence of $e^{jl\phi}$ carrying OAM
[17]	2004	Conducted the first experiment on OAM free-space optical communications
[76]	2006	Reported the generation of an OAM-carrying optical vortex in optical fibers
[62]	2007	Numerically showed that OAM can be used in the radio frequency domain
[23]	2012	Performed the first experimental test of encoding multiple channels on the same radio frequency through OAM
[80]	2013	Conducted the first OAM-MDM experiment suggesting that OAM could provide an additional degree of freedom for data multiplexing in future fiber networks
[5]	2018	Suggested a potential application that takes advantage of the OAM cone-shaped pattern in the far-field

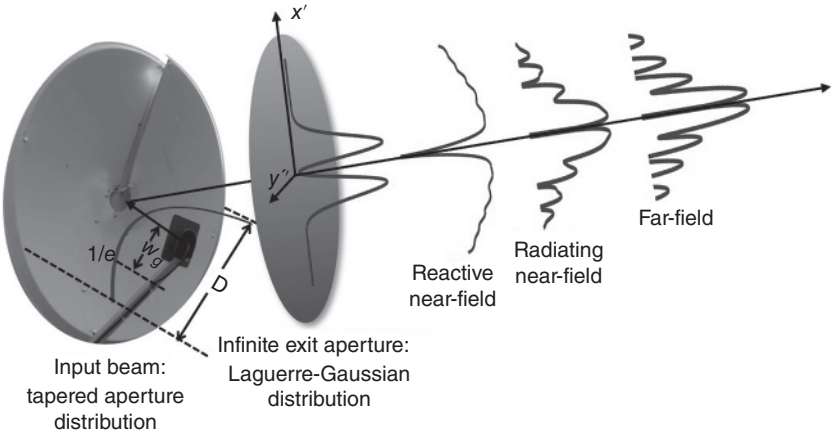

Figure 1.A.1 Schematic of the generation of OAM aperture field.

where ρ' and ϕ' are the radial and azimuthal coordinates in the cylindrical coordinate system; a is the transverse extend of the aperture field of the beam; l is the OAM order. A schematic of the generation of the OAM aperture field is shown in Figure 1.A.1. Typically, the input beam from the feed is a Gaussian-type beam with a tapered amplitude distribution. The beam waist w_g, i.e. the half-width of the normalized aperture field amplitude at $1/e$, is directly related to the OAM antenna aperture diameter D, as shown in Figure 1.A.1. For example, the equivalent beam waist in Ref. [5] was $w_g = 0.415D$ for a -12 dB taper illumination. Higher taper illumination would lead to a smaller equivalent beam waist. The role of the OAM antenna (helicoidal reflector in Figure 1.A.1) is to create the desired exit-aperture amplitude and phase distribution at the infinite exit-aperture plane. A common model for the aperture field of an OAM antenna is the Laguerre–Gaussian distribution Eq. (1.3).

The equivalent magnetic current density is calculated from [122, eq. 6-129b]:

$$\vec{M}_s = -\hat{z} \times \vec{E}(\rho', \phi') = -\hat{y} E(\rho') e^{-jl\phi'}, \quad 0 < \rho' < a. \tag{1.A.2}$$

The radiation integrals can be written as [122, eqs. 6-125c, 6-125d]:

$$L_\theta = -\cos\theta \sin\phi \int_0^a E(\rho') \left[\int_0^{2\pi} e^{-jl\phi'} e^{jk_0\rho' \sin\theta \cos(\phi - \phi')} d\phi' \right] \rho' d\rho' \tag{1.A.3}$$

$$L_\phi = -\cos\phi \int_0^a E(\rho') \left[\int_0^{2\pi} e^{-jl\phi'} e^{jk_0\rho' \sin\theta \cos(\phi - \phi')} d\phi' \right] \rho' d\rho'. \tag{1.A.4}$$

Using the integral identity [5, eq. (5)]:

$$\int_0^{2\pi} e^{-jl\phi'} e^{jk_0\rho' \sin\theta \cos(\phi - \phi')} d\phi' = 2\pi(-j)^l J_l(k_0 \sin\theta \rho') e^{-jl\phi}, \tag{1.A.5}$$

we find the expression of the far-field integrals:

$$L_\theta = -2\pi \cos\theta \sin\phi (-j)^l e^{-jl\phi} I \tag{1.A.6}$$

$$L_\phi = -2\pi \cos\phi (-j)^l e^{-jl\phi} I, \tag{1.A.7}$$

where

$$I = \int_0^a E(\rho') J_l(k_0 \sin\theta \rho') \rho' d\rho' \tag{1.A.8}$$

and $J_l(\cdot)$ is the lth order Bessel function of the first kind [21]. The expression of the far-field electric field can be written as [122, eqs. 6-122b, 6-122c]:

$$\vec{E}_{ff}(r, \theta, \phi) = \frac{jk_0 e^{-jk_0 r}}{4\pi r} \left(-\hat{\theta} L_\phi + \hat{\phi} L_\theta \right) = \frac{jk_0 e^{-jk_0 r}}{2r} - je^{-jl\phi} \left(\hat{\theta} \cos\phi - \hat{\phi} \cos\theta \sin\phi \right) I. \tag{1.A.9}$$

Note the far-field Eq. (1.A.9) maintains the $e^{-jl\phi}$ phase term.

Special Case 1: Airy Disk. The aperture field of a uniform amplitude and phase distribution is the special case of Eq. (1.A.1), where $l = 0$ (no OAM) and $E(\rho') = E_0^{AD}$. Using the integral identity [21, eq. (6.561–5)]:

$$\int_0^\delta z J_0(z) dz = \delta J_1(\delta), \tag{1.A.10}$$

we find I from Eq. (1.A.8) and the far-field expression from Eq. (1.A.9):

$$\vec{E}_{ff}^{AD}(r, \theta, \phi) = \frac{jk_0 E_0^{AD} a^2 e^{-jk_0 r}}{2r} \left(\hat{\theta} \cos\phi - \hat{\phi} \cos\theta \sin\phi \right) \frac{J_1(k_0 a \sin\theta)}{k_0 a \sin\theta}. \tag{1.A.11}$$

Special Case 2: Tapered-aperture Distribution. A physically meaningful and mathematically simple model for aperture-like antennas with uniform phase distribution is the two-parameter (2P) model [22, eq. (16)]:

$$\vec{E}^{2P}(\rho') = C + (1 - C) \left[1 - (\rho'/a)^2 \right]^P, \quad 0 < \rho' < a, \tag{1.A.12}$$

where P and C are parameters that control the shape and amplitude distribution of the circular aperture. In particular, C can be related to the edge taper by $\mathrm{ET} = 20 \log C$. A generalized three-parameter

aperture distribution model for elliptical aperture has also been developed in [123]. The far-field can be evaluated in the closed form [22, eq. (18–20)]:

$$\vec{E}_{ff}^{2P}(r,\theta,\phi) = \frac{jk_0a^2e^{-jk_0r}}{4r}\left(\hat{\theta}\cos\phi - \hat{\phi}\cos\theta\sin\phi\right)[C\Lambda_1(ka\sin\theta) + (1-C)\Lambda_{P+1}(ka\sin\theta)], \tag{1.A.13}$$

where

$$\Lambda_{P+1}(\zeta) = 2^{P+1}\Gamma(P+1)\frac{J_{P+1}(\zeta)}{\zeta^{P+1}}, \tag{1.A.14}$$

in which $\Gamma(\cdot)$ is the gamma function [21]. The far-field of the tapered-aperture distribution was studied in Section 1.2 and is shown in Figure 1.7a. The OAM tapered-aperture distribution counterpart was modeled based on Eq. (1.A.12) multiplied by the phase term $e^{-jl\phi}$:

$$\vec{E}_{OAM}^{2P}(\rho') = \left\{C + (1-C)\left[1-(\rho'/a)^2\right]^P\right\}e^{-jl\phi}, \quad 0 < \rho' < a. \tag{1.A.15}$$

The changes of amplitude pattern shape based on the aperture field of Eq. (1.A.15) from the reactive near-field toward the far-field were studied in Section 1.2 and are shown in Figure 1.7b.

Special Case 3: Laguerre–Gaussian beam. The aperture field of the Laguerre–Gaussian beams is given by Eq. (1.3). Using the integral identity [21, eq. (7.421-4)]

$$\int_0^\infty x^{\nu+1}e^{-\beta x^2}L_n^\nu(ax^2)J_\nu(xy) = 2^{-\nu-1}\beta^{-\nu-n-1}(\beta-a)^n y^\nu e^{-\frac{y^2}{4\beta}}L_n^\nu\left[\frac{ay^2}{4\beta(a-\beta)}\right], \tag{1.A.16}$$

we find I from Eq. (1.A.8) and the far-field expression from Eq. (1.A.9):

$$\begin{aligned}\vec{E}_{ff}^{LG}(r,\theta,\phi) = {} & \frac{jk_0E_0^{LG}e^{-jk_0r}}{4\pi r}\left(\hat{\theta}\cos\phi - \hat{\phi}\cos\theta\sin\phi\right)w_g(-1)^p(-j)^l \\ & \times\sqrt{\frac{2\pi p!}{(p+|l|)!}}\left(\frac{sgn(l)\Psi}{\sqrt{2}}\right)^{|l|}e^{-\frac{\Psi^2}{4}}L_p^{|l|}\left(\frac{\Psi^2}{2}\right)e^{-jl\phi},\end{aligned} \tag{1.A.17}$$

where $\Psi = k_0w_g\sin\theta$. For the definition of w_g refer to the first paragraph of the appendix and Figure 1.A.1. The previous discussion refers to the far-field where the radiation integral can be found in closed form. The near-field calculation using the Fresnel–Kirchhoff diffraction integral [24] was carried out numerically in Section 1.2 and the results are shown in Figure 1.7.

References

1 Poynting, J.H. (1909). The wave motion of a revolving shaft, and a suggestion as to the angular momentum in a beam of circularly polarised light. *Proceedings of the Royal Society of London* **82** (557): 560–567.

2 Beth, R.A. (1936). Mechanical detection and measurement of the angular momentum of light. *Physical Review* **50**: 115–125.

3 Allen, L., Beijersbergen, M.W., Spreeuw, R., and Woerdman, J. (1992). Orbital angular momentum of light and the transformation of Laguerre-Gaussian laser modes. *Physical Review A* **45** (11): 8185.

4 Drysdale, T.D., Allen, B., Stevens, C. et al. (2018). How orbital angular momentum modes are boosting the performance of radio links. *IET Microwaves, Antennas & Propagation* **12** (10): 1625–1632.

5 Veysi, M., Guclu, C., Capolino, F., and Rahmat-Samii, Y. (2018). Revisiting orbital angular momentum beams: Fundamentals, reflectarray generation, and novel antenna applications. *IEEE Antennas and Propagation Magazine* **60** (2): 68–81.

6 Cheng, W., Zhang, W., Jing, H. et al. (2019). Orbital angular momentum for wireless communications. *IEEE Wireless Communications* **26** (1): 100–107.

7 Gori, F., Guattari, G., and Padovani, C. (1987). Bessel-Gauss beams. *Optics Communications* **64** (6): 491–495.

8 Karimi, E., Zito, G., Piccirillo, B. et al. (2007). Hypergeometric-Gaussian modes. *Optics Letters* **32** (21): 3053–3055.

9 Maurer, C., Jesacher, A., Fürhapter, S. et al. (2007). Tailoring of arbitrary optical vector beams. *New Journal of Physics* **9** (3): 78.

10 Allen, L., Padgett, M., and Babiker IV, M. (1999). The orbital angular momentum of light, Progress in Optics. *Elsevier* **39**: 291–372.

11 Willner, A.E., Huang, H., Yan, Y. et al. (2015). Optical communications using orbital angular momentum beams. *Advances in Optics and Photonics* **7** (1): 66–106.

12 Padgett, M.J., Miatto, F.M., Lavery, M.P. et al. (2015). Divergence of an orbital-angular-momentum-carrying beam upon propagation. *New Journal of Physics* **17** (2): 023011.

13 Beijersbergen, M., Coerwinkel, R., Kristensen, M., and Woerdman, J. (1994). Helical-wavefront laser beams produced with a spiral phaseplate. *Optics Communications* **112** (5-6): 321–327.

14 Trichili, A., Rosales-Guzmán, C., Dudley, A. et al. (2016). Optical communication beyond orbital angular momentum. *Scientific Reports* **6**: 27674.

15 Oldoni, M., Spinello, F., Mari, E. et al. (2015). Space-division demultiplexing in orbital-angular-momentum-based mimo radio systems. *IEEE Transactions on Antennas and Propagation* **63** (10): 4582–4587.

16 Djordjevic, I.B. (2011). Deep-space and near-earth optical communications by coded orbital angular momentum (OAM) modulation. *Optics Express* **19** (15): 14277–14289.

17 Gibson, G., Courtial, J., Padgett, M.J. et al. (2004). Free-space information transfer using light beams carrying orbital angular momentum. *Optics Express* **12** (22): 5448–5456.

18 Ge, X., Zi, R., Xiong, X. et al. (2017). Millimeter wave communications with OAM-SM scheme for future mobile networks. *IEEE Journal on Selected Areas in Communications* **35** (9): 2163–2177.

19 Turnbull, G., Robertson, D., Smith, G. et al. (1996). The generation of free-space Laguerre-Gaussian modes at millimetre-wave frequencies by use of a spiral phaseplate. *Optics Communications* **127** (4-6): 183–188.

20 Yao, A.M. and Padgett, M.J. (2011). Orbital angular momentum: origins, behavior and applications. *Advances in Optics and Photonics* **3** (2): 161–204.

21 Gradshteyn, I.S. and Ryzhik, I.M. (2014). *Table of Integrals, Series, and Products*, 7e. Academic press.

22 Rahmat-Samii, Y. (1988). Reflector antennas. In: *Antenna Handbook: Theory, Applications, and Design* (eds. S.W. Lee and Y.T. Lo), 949–1072. Boston, MA: Springer US.

23 Tamburini, F., Mari, E., Sponselli, A. et al. (2012). Encoding many channels on the same frequency through radio vorticity: first experimental test. *New Journal of Physics* **14** (3): 033001.

24 Born, M. and Wolf, E. (2013). *Principles of Optics: Electromagnetic Theory of Propagation, Interference and Diffraction of Light*, 6e. Elsevier.

25 Balanis, C.A. (2016). *Antenna Theory: Analysis and Design*, 4e. John Wiley & Sons.

26 Friis, H.T. (1946). A note on a simple transmission formula. *Proceedings of the IRE* **34** (5): 254–256.

27 Cho, Y.H. and Byun, W.J. (2019). Generalized friis transmission equation for orbital angular momentum radios. *IEEE Transactions on Antennas and Propagation* **67** (4): 2423–2429.

28 Nguyen, D.K., Pascal, O., Sokoloff, J. et al. (2015). Antenna gain and link budget for waves carrying orbital angular momentum. *Radio Science* **50** (11): 1165–1175.

29 D. K. Nguyen, O. Pascal, J. Sokoloff, et al. (2014). Discussion about the link budget for electromagnetic wave with orbital angular momentum, *The 8th European Conference on Antennas and Propagation (EuCAP 2014)*. IEEE, pp. 1117–1121.

30 Cagliero, A., De Vita, A., Gaffoglio, R., and Sacco, B. (2015). A new approach to the link budget concept for an OAM communication link. *IEEE Antennas and Wireless Propagation Letters* **15**: 568–571.

31 Craeye, C. (2015). On the transmittance between OAM antennas. *IEEE Transactions on Antennas and Propagation* **64** (1): 336–339.

32 C. Rui, Z. Hong, M. Marco, et al. (2019). Orbital angular momentum waves: Generation, detection and emerging applications, *arXiv preprint arXiv:1903.07818*.

33 Edfors, O. and Johansson, A.J. (2011). Is orbital angular momentum (OAM) based radio communication an unexploited area? *IEEE Transactions on Antennas and Propagation* **60** (2): 1126–1131.

34 Tamagnone, M., Craeye, C., and Perruisseau-Carrier, J. (2012). Comment on 'Encoding many channels on the same frequency through radio vorticity: first experimental test'. *New Journal of Physics* **14** (11): 118001.

35 Morabito, A.F., Di Donato, L., and Isernia, T. (2018). Orbital angular momentum antennas: Understanding actual possibilities through the aperture antennas theory. *IEEE Antennas and Propagation Magazine* **60** (2): 59–67.

36 Xie, G., Li, L., Ren, Y. et al. (2015). Performance metrics and design considerations for a free-space optical orbital-angular-momentum multiplexed communication link. *Optica* **2** (4): 357–365.

37 Gao, X., Song, X., Zheng, Z. et al. (2020). Misalignment measurement of orbital angular momentum signal based on spectrum analysis and image processing. *IEEE Transactions on Antennas and Propagation* **68** (1): 521–526.

38 Anguita, J.A., Neifeld, M.A., and Vasic, B.V. (2008). Turbulence-induced channel crosstalk in an orbital angular momentum-multiplexed free-space optical link. *Applied Optics* **47** (13): 2414–2429.

39 Tyler, G.A. and Boyd, R.W. (2009). Influence of atmospheric turbulence on the propagation of quantum states of light carrying orbital angular momentum. *Optics Letters* **34** (2): 142–144.

40 Paterson, C. (2005). Atmospheric turbulence and orbital angular momentum of single photons for optical communication. *Physical Review Letters* **94** (15): 153901.

41 Rodenburg, B., Lavery, M.P., Malik, M. et al. (2012). Influence of atmospheric turbulence on states of light carrying orbital angular momentum. *Optics Letters* **37** (17): 3735–3737.

42 Ren, Y., Huang, H., Xie, G. et al. (2013). Atmospheric turbulence effects on the performance of a free space optical link employing orbital angular momentum multiplexing. *Optics Letters* **38** (20): 4062–4065.

43 Malik, M., O'Sullivan, M., Rodenburg, B. et al. (2012). Influence of atmospheric turbulence on optical communications using orbital angular momentum for encoding. *Optics Express* **20** (12): 13195–13200.

44 Chaibi, A., Mafusire, C., and Forbes, A. (2013). Propagation of orbital angular momentum carrying beams through a perturbing medium. *Journal of Optics* **15** (10): 105706.

45 Trichili, A., Salem, A.B., Dudley, A. et al. (2016). Encoding information using Laguerre Gaussian modes over free space turbulence media. *Optics Letters* **41** (13): 3086–3089.

46 Willner, A.E., Ren, Y., Xie, G. et al. (2017). Recent advances in high-capacity free-space optical and radio-frequency communications using orbital angular momentum multiplexing. *Philosophical Transactions of the Royal Society A: Mathematical, Physical and Engineering Sciences* **375** (2087): 20150439.

47 Yan, Y., Li, L., Xie, G. et al. (2016). Multipath effects in millimetre-wave wireless communication using orbital angular momentum multiplexing. *Scientific Reports* **6**: 33482.

48 Vicente-Lozano, M., Franceschetti, G., Ares-Pena, F.J., and Moreno-Piquero, E. (2002). Analysis and synthesis of a printed array for satellite communication with moving vehicles. *IEEE Transactions on Antennas and Propagation* **50** (11): 1555–1559.

49 Pan, Y.-M. and Leung, K.W. (2012). Wideband circularly polarized dielectric bird-nest antenna with conical radiation pattern. *IEEE Transactions on Antennas and Propagation* **61** (2): 563–570.

50 Lau, K. and Luk, K. (2006). A wideband circularly polarized conical-beam patch antenna. *IEEE Transactions on Antennas and Propagation* **54** (5): 1591–1594.

51 Lin, W. and Wong, H. (2014). Circularly polarized conical-beam antenna with wide bandwidth and low profile. *IEEE Transactions on Antennas and Propagation* **62** (12): 5974–5982.

52 Kai, C., Huang, P., Shen, F. et al. (2017). Orbital angular momentum shift keying based optical communication system. *IEEE Photonics Journal* **9** (2): 1–10.

53 Trichili, A., Park, K.-H., Zghal, M. et al. (2019). Communicating using spatial mode multiplexing: Potentials, challenges and perspectives. *IEEE Communications Surveys & Tutorials* **21** (4): 3175–3203.

54 Krenn, M., Fickler, R., Fink, M. et al. (2014). Communication with spatially modulated light through turbulent air across Vienna. *New Journal of Physics* **16** (11): 113028.

55 Krenn, M., Handsteiner, J., Fink, M. et al. (2016). Twisted light transmission over 143 km. *Proceedings of the National Academy of Sciences* **113** (48): 13648–13653.

56 Molisch, A. (2005). *Wireless Communications*. Wiley-IEEE Press.

57 Goldsmith, A. (2005). *Wireless Communications*. USA: Cambridge University Press.

58 Lee, D., Sasaki, H., Fukumoto, H. et al. (2017). Orbital angular momentum (OAM) multiplexing: An enabler of a new era of wireless communications. *IEICE Transactions on Communications* **100** (7): 1044–1063.

59 Cheng, W., Zhang, W., Jing, H. et al. (2018). Orbital angular momentum for wireless communications. *IEEE Wireless Communications* **26** (1): 100–107.

60 Huang, H., Xie, G., Yan, Y. et al. (2014). 100 Tbit s^{-1} free-space data link enabled by three-dimensional multiplexing of orbital angular momentum, polarization, and wavelength. *Optics Letters* **39** (2): 197–200.

61 Wang, J., Yang, J.-Y., Fazal, I.M. et al. (2012). Terabit free-space data transmission employing orbital angular momentum multiplexing. *Nature Photonics* **6** (7): 488.

62 Thidé, B., Then, H., Sjöholm, J. et al. (2007). Utilization of photon orbital angular momentum in the low-frequency radio domain. *Physical Review Letters* **99** (8): 087701.

63 Zhang, W., Zheng, S., Hui, X. et al. (2016). Mode division multiplexing communication using microwave orbital angular momentum: An experimental study. *IEEE Transactions on Wireless Communications* **16** (2): 1308–1318.

64 Yan, Y., Xie, G., Lavery, M.P. et al. (2014). High-capacity millimetre-wave communications with orbital angular momentum multiplexing. *Nature Communications* **5**: 4876.

65 Willner, A. (2019). *Optical Fiber Telecommunications*, vol. **11**. Academic Press.

66 Cisco Global Cloud Index: Forecast and Methodology, 2016–2021 White Paper - Cisco, https://www.cisco.com/c/en/us/solutions/collateral/service-provider/global-cloud-index-gci/white-paper-c11-738085.html#_Toc503317520 (accessed 2 March 2020).

67 Richardson, D., Fini, J., and Nelson, L.E. (2013). Space-division multiplexing in optical fibres. *Nature Photonics* **7** (5): 354.

68 Saridis, G.M., Alexandropoulos, D., Zervas, G., and Simeonidou, D. (2015). Survey and evaluation of space division multiplexing: From technologies to optical networks. *IEEE Communications Surveys & Tutorials* **17** (4): 2136–2156.

69 Rusch, L.A., Rad, M., Allahverdyan, K. et al. (2018). Carrying data on the orbital angular momentum of light. *IEEE Communications Magazine* **56** (2): 219–224.

70 Li, G., Bai, N., Zhao, N., and Xia, C. (2014). Space-division multiplexing: the next frontier in optical communication. *Advances in Optics and Photonics* **6** (4): 413–487.

71 Ramachandran, S. and Kristensen, P. (2013). Optical vortices in fiber. *Nanophotonics* **2** (5-6): 455–474.

72 Li, Y., Jin, L., Wu, H. et al. (2017). Superposing multiple LP modes with microphase difference distributed along fiber to generate oam mode. *IEEE Photonics Journal* **9** (2): 1–9.

73 Ramachandran, S., Gregg, P., Kristensen, P., and Golowich, S. (2015). On the scalability of ring fiber designs for OAM multiplexing. *Optics Express* **23** (3): 3721–3730.

74 Chen, S. and Wang, J. (2017). Theoretical analyses on orbital angular momentum modes in conventional graded-index multimode fibre. *Scientific Reports* **7** (1): 1–15.

75 Li, S. and Wang, J. (2014). A compact trench-assisted multi-orbital-angular-momentum multi-ring fiber for ultrahigh-density space-division multiplexing (19 rings × 22 modes). *Scientific Reports* **4**: 3853.

76 Dashti, P.Z., Alhassen, F., and Lee, H.P. (2006). Observation of orbital angular momentum transfer between acoustic and optical vortices in optical fiber. *Physical Review Letters* **96** (4): 043604.

77 Bozinovic, N., Kristensen, P., and Ramachandran, S. (2011). Long-range fiber-transmission of photons with orbital angular momentum. In: *CLEO: Science and Innovations*, CTuB1. Optical Society of America.

78 Bozinovic, N., Golowich, S., Kristensen, P., and Ramachandran, S. (2012). Control of orbital angular momentum of light with optical fibers. *Optics Letters* **37** (13): 2451–2453.

79 Ramachandran, S., Bozinovic, N., Gregg, P. et al. (2012). Optical vortices in fibres: A new degree of freedom for mode multiplexing. In: *2012 38th European Conference and Exhibition on Optical Communications*, 1–3. IEEE.

80 Bozinovic, N., Yue, Y., Ren, Y. et al. (2013). Terabit-scale orbital angular momentum mode division multiplexing in fibers. *Science* **340** (6140): 1545–1548.

81 Ingerslev, K., Gregg, P., Galili, M. et al. (2018). 12 mode, WDM, MIMO-free orbital angular momentum transmission. *Optics Express* **26** (16): 20225–20232.

82 Huang, H., Milione, G., Lavery, M.P. et al. (2015). Mode division multiplexing using an orbital angular momentum mode sorter and MIMO-DSP over a graded-index few-mode optical fibre. *Scientific Reports* **5** (1): 1–7.

83 Zhu, L., Wang, A., Chen, S. et al. (2017). Orbital angular momentum mode groups multiplexing transmission over 2.6-km conventional multi-mode fiber. *Optics Express* **25** (21): 25637–25645.

84 Wang, A., Zhu, L., Wang, L. et al. (2018). Directly using 8.8-km conventional multi-mode fiber for 6-mode orbital angular momentum multiplexing transmission. *Optics Express* **26** (8): 10038–10047.

85 Zhu, L., Wang, A., Chen, S. et al. (2018). Orbital angular momentum mode multiplexed transmission in heterogeneous few-mode and multi-mode fiber network. *Optics Letters* **43** (8): 1894–1897.

86 Li, S. and Wang, J. (2013). Multi-orbital-angular-momentum multi-ring fiber for high-density space-division multiplexing. *IEEE Photonics Journal* **5** (5): 7101007–7101007.

87 Li, S. and Wang, J. (2015). Supermode fiber for orbital angular momentum (OAM) transmission. *Optics Express* **23** (14): 18736–18745.

88 Papathanasopoulos, A., Rahmat-Samii, Y., Garcia, N., and Chisum, J.D. (2020). A novel collapsible flat-layered metamaterial gradient-refractive-index (GRIN) lens antenna. *IEEE Transactions on Antennas and Propagation* **68** (3): 1312–1321.

89 Wei, X., Liu, C., Niu, L. et al. (2015). Generation of arbitrary order Bessel beams via 3D printed axicons at the terahertz frequency range. *Applied Optics* **54** (36): 10641–10649.

90 Zhang, C. and Ma, L. (2016). Millimetre wave with rotational orbital angular momentum. *Scientific Reports* **6** (1): 1–8.

91 L. Zhu, X. Wei, J. Wang, et al. (2014). Experimental demonstration of basic functionalities for 0.1-THz orbital angular momentum (OAM) communications, *Optical Fiber Communication Conference,* OSA Technical Digest (online) (Optical Society of America, 2014), paper M3K.

92 Byun, W.-J., Lee, Y.-S., Kim, B.S. et al. (2015). Simple generation of orbital angular momentum modes with azimuthally deformed Cassegrain subreflector. *Electronics Letters* **51** (19): 1480–1482.

93 Mari, E., Spinello, F., Oldoni, M. et al. (2014). Near-field experimental verification of separation of OAM channels. *IEEE Antennas and Wireless Propagation Letters* **14**: 556–558.

94 Byun, W.J., Kim, K.S., Kim, B.S. et al. (2016). Multiplexed Cassegrain reflector antenna for simultaneous generation of three orbital angular momentum (OAM) modes. *Scientific Reports* **6**: 27339.

95 Cheng, L., Hong, W., and Hao, Z.-C. (2014). Generation of electromagnetic waves with arbitrary orbital angular momentum modes. *Scientific Reports* **4** (1): 1–5.

96 Qin, F., Wan, L., Li, L. et al. (2018). A transmission metasurface for generating OAM beams. *IEEE Antennas and Wireless Propagation Letters* **17** (10): 1793–1796.

97 Hui, X., Zheng, S., Hu, Y. et al. (2015). Ultralow reflectivity spiral phase plate for generation of millimeter-wave OAM beam. *IEEE Antennas and Wireless Propagation Letters* **14**: 966–969.

98 Chen, Y., Zheng, S., Li, Y. et al. (2015). A flat-lensed spiral phase plate based on phase-shifting surface for generation of millimeter-wave OAM beam. *IEEE Antennas and Wireless Propagation Letters* **15**: 1156–1158.

99 A. Bennis, R. Niemiec, C. Brousseau, et al. (2013). Flat plate for OAM generation in the millimeter band, *2013 7th European Conference on Antennas and Propagation (EuCAP)*. IEEE, pp. 3203–3207.

100 Niemiec, R., Brousseau, C., Mahdjoubi, K. et al. (2014). Characterization of an OAM flat-plate antenna in the millimeter frequency band. *IEEE Antennas and Wireless Propagation Letters* **13**: 1011–1014.

101 Tamburini, F., Mari, E., Thidé, B. et al. (2011). Experimental verification of photon angular momentum and vorticity with radio techniques. *Applied Physics Letters* **99** (20): 204102.

102 Bai, Q., Tennant, A., and Allen, B. (2014). Experimental circular phased array for generating OAM radio beams. *Electronics Letters* **50** (20): 1414–1415.

103 Liu, K., Liu, H., Qin, Y. et al. (2016). Generation of OAM beams using phased array in the microwave band. *IEEE Transactions on Antennas and Propagation* **64** (9): 3850–3857.

104 Kang, L., Li, H., Zhou, J. et al. (2019). A mode-reconfigurable orbital angular momentum antenna with simplified feeding scheme. *IEEE Transactions on Antennas and Propagation* **67** (7): 4866–4871.

105 Liu, Q., Chen, Z.N., Liu, Y. et al. (2018). Circular polarization and mode reconfigurable wideband orbital angular momentum patch array antenna. *IEEE Transactions on Antennas and Propagation* **66** (4): 1796–1804.

106 Zhao, M., Gao, X., Xie, M. et al. (2018). Generation of coupled radio frequency orbital angular momentum beam with an optical-controlled circular antenna array. *Optics Communications* **426**: 126–129.

107 Gong, Y., Wang, R., Deng, Y. et al. (2017). Generation and transmission of OAM-carrying vortex beams using circular antenna array. *IEEE Transactions on Antennas and Propagation* **65** (6): 2940–2949.

108 Yuan, T., Cheng, Y., Wang, H.-Q., and Qin, Y. (2016). Generation of OAM radio beams with modified uniform circular array antenna. *Electronics Letters* **52** (11): 896–898.

109 Lin, M., Gao, Y., Liu, P., and Liu, J. (2017). Theoretical analyses and design of circular array to generate orbital angular momentum. *IEEE Transactions on Antennas and Propagation* **65** (7): 3510–3519.

110 F. E. Mahmouli and S. Walker. (2012). Orbital angular momentum generation in a 60GHz wireless radio channel, *2012 20th Telecommunications Forum (TELFOR)*, Belgrade, Serbia: IEEE, (20–22 November 2012).

111 Bazhenov, V.Y., Vasnetsov, M., and Soskin, M. (1990). Laser beams with screw dislocations in their wavefronts. *JETP Letter* **52** (8): 429–431.

112 Heckenberg, N., McDuff, R., Smith, C., and White, A. (1992). Generation of optical phase singularities by computer-generated holograms. *Optics Letters* **17** (3): 221–223.

113 Arlt, J., Dholakia, K., Allen, L., and Padgett, M. (1998). The production of multiringed Laguerre–Gaussian modes by computer-generated holograms. *Journal of Modern Optics* **45** (6): 1231–1237.

114 Meng, X.-S., Wu, J.-J., Wu, Z.-S. et al. (2018). Design of multiple-polarization reflectarray for orbital angular momentum wave in radio frequency. *IEEE Antennas and Wireless Propagation Letters* **17** (12): 2269–2273.

115 Yu, S., Li, L., Shi, G. et al. (2016). Generating multiple orbital angular momentum vortex beams using a metasurface in radio frequency domain. *Applied Physics Letters* **108** (24): 241901.

116 Chen, G.-T., Jiao, Y.-C., and Zhao, G. (2018). A reflectarray for generating wideband circularly polarized orbital angular momentum vortex wave. *IEEE Antennas and Wireless Propagation Letters* **18** (1): 182–186.

117 Huang, H.-F. and Li, S.-N. (2019). High-efficiency planar reflectarray with small-size for OAM generation at microwave range. *IEEE Antennas and Wireless Propagation Letters* **18** (3): 432–436.

118 Marrucci, L., Karimi, E., Slussarenko, S. et al. (2011). Spin-to-orbital conversion of the angular momentum of light and its classical and quantum applications. *Journal of Optics* **13** (6): 064001.

119 Pan, Y., Zheng, S., Zheng, J. et al. (2016). Generation of orbital angular momentum radio waves based on dielectric resonator antenna. *IEEE Antennas and Wireless Propagation Letters* **16**: 385–388.

120 Zheng, S., Hui, X., Jin, X. et al. (2015). Transmission characteristics of a twisted radio wave based on circular traveling-wave antenna. *IEEE Transactions on Antennas and Propagation* **63** (4): 1530–1536.

121 Wu, J., Zhang, Z., Ren, X. et al. (2019). A broadband electronically mode-reconfigurable orbital angular momentum metasurface antenna. *IEEE Antennas and Wireless Propagation Letters* **18** (7): 1482–1486.

122 Balanis, C.A. (2012). *Advanced Engineering Electromagnetics*, 2e. John Wiley & Sons.

123 Duan, D.-W. and Rahmat-Samii, Y. (1992). A generalized three-parameter (3-P) aperture distribution for antenna applications. *IEEE Transactions on Antennas and Propagation* **40** (6): 697–713.